

Exact quantum dynamics of methanol: full-dimensional *ab initio* potential energy surface of spectroscopic quality and variational vibrational states

Ayaki Sunaga,¹ Tibor Györi,^{2,*} Gábor Czako,^{2,†} and Edit Mátyus^{1,‡}

¹*ELTE, Eötvös Loránd University, Institute of Chemistry,
Pázmány Péter sétány 1/A 1117 Budapest, Hungary*

²*MTA-SZTE Lendület “Momentum” Computational Reaction Dynamics Research Group,
Interdisciplinary Excellence Centre and Department of Physical Chemistry and Materials Science,
Institute of Chemistry, University of Szeged,
Rerrich Béla tér 1, Szeged H-6720, Hungary*

(Dated: August 5, 2025)

The methanol molecule is a sensitive probe of astrochemistry, astrophysics, and fundamental physics. The first-principles elucidation and prediction of its rotation-torsional-vibrational motions are enabled in this work by the computation of a full-dimensional, *ab initio* potential energy surface (PES) and numerically exact quantum dynamics. An active-learning approach is used to sample explicitly correlated coupled-cluster electronic energies, and the datapoints are fitted with permutationally invariant polynomials to obtain a spectroscopic-quality PES representation. Variational vibrational energies and corresponding tunnelling splittings are computed up to the first overtone of the C-O stretching mode by direct numerical solution of the vibrational Schrödinger equation with optimal internal coordinates and efficient basis and grid truncation techniques. As a result, the computed vibrational band origins finally agree with experiment within 5 cm^{-1} , allowing for the exploration of the large-amplitude quantum mechanical motion and tunnelling splittings coupled with the small-amplitude vibrational dynamics. These developments open the route towards simulating rovibrational spectra used to probe methanol in outer space and in precision science laboratories, as well as for probing interactions with external magnetic fields.

I. INTRODUCTION

CH_3OH is the smallest alcohol and a prototype of quantum mechanical large-amplitude motions and corresponding tunnelling splittings. It is also one of the most abundant organic molecules in the Universe, which explains its importance in astrophysics. Its particular rovibrational level structure, dominated by the large-amplitude internal rotation, has been proposed as a sensitive probe for the proton-to-electron mass ratio variation at astronomical scales^{1–4}. Most recently, the internal rotation of substituted methanol compounds was considered for enhanced parity-violating effects⁵. The hyperfine-Zeeman splittings of methanol, based on a reduced dimensionality model, were used to measure (weak) magnetic fields on distant astronomical objects⁶. The methanol molecule also plays a central role in astrochemistry; the ratio of its isotopologues has been studied in the context of the formation of organic compounds in outer space^{7–12}.

Methanol has been a prototype for fundamental spectroscopy and quantum nuclear motion theory, mostly for the non-trivial couplings of its small-amplitude degrees of freedom, the large-amplitude internal rotation, and the overall molecular rotation. Its fundamental vibrations were detected with infrared¹³ and Raman¹⁴ spectroscopy already in 1937–38 and were assigned based on the C_s point group^{15–19}. The torsion-rotation coupling was later analysed in a series of work^{20–25}, recently followed by high-precision spectroscopy using an ultra-narrow quantum cascade laser²⁶. The molecular symmetry group²⁷ can be used for a more complete understanding of the degenerate and tunnelling splitting levels, but arguments were put forward for using the complete permutation-inversion group^{28,29}, so as not to lose important parity information of the eigenstates.

We also note that combination bands of methanol have been studied with matrix isolation spectroscopy^{30–32}. Regarding (rectilinear) normal coordinate computations, which are limited to describing small-amplitude vibrations, we mention vibrational self-consistent field (VSCF) and related vibrational configuration interaction-type (VCI) computations^{33–37}. The computed VCI

* tibor.gyori@chem.u-szeged.hu

† gczako@chem.u-szeged.hu

‡ edit.matyus@ttk.elte.hu

fundamental-mode energies, not considering the torsional motion and the tunneling splittings, agree well with the matrix isolation data³⁸. Further computational methodologies were developed using a tree-tensor-network-state ansatz based on the state-shifted Hamiltonian³⁹.

There has been recent progress in a numerically exact solution of the rovibrational Schrödinger equation on an *ab initio* (or perhaps spectroscopically refined) potential energy surface (PES), allowing also for large-amplitude motions (LAMs)^{40–44}. In relation to scaling up the vibrational dimensionality, we mention recent developments in collocation^{45,46} and contraction^{47–49}. The full-dimensional (12D) variational computation of methanol was first reported by Lauvergnat and Nauts^{50,51}. In our group, 12D variational computations were also performed using the GENIUSH-Smolyak approach for methane-atom(ion) complexes^{52–55}, by including the atom(ion)-methane large-amplitude relative motions fully coupled with the methane’s small-amplitude internal vibrations. These developments were followed by applications for the formic acid molecule^{56,57} and methanol⁵⁸ using path-following curvilinear normal coordinates. The efficient basis and grid truncation made it possible to converge the vibrational energies of methanol (12D) within 1-2 cm^{-1} with respect to the vibrational basis and grid up to the combination bands at ca. 2200 cm^{-1} beyond the zero-point vibrational energy, ZPVE. In this range, the large, 10-20 cm^{-1} deviations from experiment indicated that the underlying PES⁵⁹ (henceforth labeled as PES13) required improvement⁵⁸.

Regarding the PES development, the challenging aspects of treating the torsional motion are (i) accounting for the three equivalent minima and (ii) covering a wider geometry region beyond small-amplitude motions (SAMs) about local minima. A solution for (i) has been well established in the community: the permutation-invariant-polynomial (PIP) method, which was initially reported by Joel Bowman’s group^{60–62} and is continuing to see recent improvements^{63–67}. Solving (ii) involves expanding the region of interest in the 12D hypervolume, which necessitates the use of either increasingly many *ab initio* energies to adequately sample the hypervolume or some sparse sampling technique that takes advantage of the fitting method’s ability to interpolate between the points of the fitting set. Since high-accuracy *ab initio* energies are computationally expensive, the latter approach is preferable; however, the practical implementation details remain challenging and will be addressed in this work.

One of the strategies for efficiently choosing geometry points for the fitting is the active-learning-like approach of the ROBOSURFER program system⁶⁸. The accuracy of PESs developed with the PIP fitting has been demonstrated^{54,55} from the equilibrium structures up to the methane-atom(ion) dissociation limits of the methane complexes $\text{CH}_4\cdot\text{Ar}$ and $\text{CH}_4\cdot\text{F}^-$, of which the latter applications used ROBOSURFER. In this study, we use and improve upon this combination of methods to obtain a new PES for methanol, which is reported in the first part of the paper.

II. CONSTRUCTION OF THE POTENTIAL ENERGY SURFACE

A. Background and methodology

The concept of a PES arises from the Born-Oppenheimer approximation. For every molecular geometry, there is a potential energy value that can (in principle) be obtained by solving the Schrödinger equation of the electrons. While no analytical solution is known for many-electron systems and numerically exact solutions are unfeasible in most cases, modern quantum chemistry offers a number of efficient and accurate approximations. These typically involve the simultaneous use of: (I) an approximate many-electron wavefunction where the correlated motion of electrons stemming from electron-electron repulsion is only partially considered and relativistic effects are either ignored or approximated, and (II) a finite set of carefully optimized basis functions which are linearly combined to construct the molecular orbitals.

In this study, we combine a well-established coupled-cluster approximation of electronic motion, CCSD(T)-F12b⁶⁹, with the cc-pVTZ-F12⁷⁰ basis set to compute potential energy values at a reasonable computational cost.

In principle, a variational vibrational computation could be carried out by querying the *ab initio* energy computation method described above at every quadrature point of the numerical integration grid used for computing the matrix elements of the vibrational Hamiltonian. But in practice, this would be prohibitively slow, as the potential energy is required at (hundreds of) millions of geometries, and each *ab initio* energy may take a couple of minutes of CPU time.

Therefore, to make the *ab initio* computation of (ro)vibrational energy levels possible, another layer of approximation needs to be introduced: a surrogate model PES, fitted to a limited number of *ab initio* energies.

In this study, we use the Braams–Bowman implementation of permutationally invariant polynomials (PIP)⁶¹ for fitting. Briefly, the polynomials are expanded in terms of Morse variables

$$y_{ij} = \exp(-r_{ij}/a), \quad (1)$$

where r_{ij} is the distance between atoms i and j and a is a distance transformation parameter. The number of coefficients (and as a result, the flexibility of the fitting function) is primarily controlled by limiting the degrees of the polynomials, as per standard practice. The energy expression of the PES is

$$E = \sum_{k=1}^Z c_k T_k M_k, \quad (2)$$

where Z is the number of permutationally invariant monomials, while c_k and T_k are the coefficient and monomial prefactor of the k -th monomial M_k , respectively. The PIP method ensures that the values of the energy returned by the PES function are invariant to any permutation of like atoms, in our case, all four H-atoms. A special feature of the PIP implementation used in this study is the ability to increase the fitting function flexibility by adding extra polynomials that are restricted in the number of atomic positions they are permitted to depend on. We refer to these as ‘extra q -body polynomials,’ and we utilise extra 2-, 3-, and 4-body polynomials in the functional form of our new potential energy surface (PES). These extra polynomials and the main polynomial can each use different values for a , Eq. (1), to achieve optimal fitting of the *ab initio* energy-geometry pairs in the fitting set. The polynomial coefficients are obtained through weighted linear least squares (LLS) fitting; the weighting function is provided in Eq. S3 of the Supplementary Material.

For constructing the fitting set, we used the ROBOSURFER program system⁶⁸, and for computing the required *ab initio* energies, we used the MOLPRO^{71–74} quantum chemistry package. Without going into the details of its operation, ROBOSURFER automates the development of PESs through an iterative, active-learning-like process, which gradually expands the fitting set with additional samples (geometry-energy pairs) until the quality of the fitted PES is judged to be satisfactory.

For the PES development, we have taken the approach of starting with a small fitting set, low degree polynomials, a high threshold (in terms of weighted error) for adding new geometries to the fitting set (E_{targ}), and gradually increasing both the flexibility of the fitting function and the accuracy we demand from the PES, as the fitting set grew. In addition to readjusting the parameters of the automated PES development process multiple times, we have also, on a handful of occasions, manually injected geometries into the development process, which were sampled around outliers in the fit. The PES development was started from a fitting set of 530 geometries, $E_{\text{targ}} = 1$ kcal/mol (349.8 cm⁻¹), a 4th degree polynomial fit and no extra monomials, resulting in 317 polynomial coefficients. By the end of the PES development, the fitting set grew to 39 401 geometries, E_{targ} was lowered to 0.05 kcal/mol (17.5 cm⁻¹), and the complexity of the fitting function was increased to the state shown in Table I. Further details of the fitting and PES development methods, as well as a highly detailed account of the progress of PES development and fitting error minimisation efforts, are provided in Section S1 of the Supplementary Material.

B. Properties and validation of the final PES

Our new PES, named PES25, is the result of fitting the final geometry set of 39 401 points with the PIP method and the parameters shown in Table I, yielding 9652 polynomial coefficients. For numerical stability reasons discussed in Section S2 of the Supplementary Material, we obtained the final coefficient values of PES25 using the DGELSY linear least squares solver, which is a LAPACK subroutine⁷⁵. This results in slightly higher fitting errors, but produces a PES with smoother derivatives.

Our fidelity assessment of the fit is summarised in Table II. The RMS fitting error of PES25 over its fitting set, 27.3 cm⁻¹, is noticeably higher than those of our previous spectroscopic PIP-PESs; e.g., the RMSEs of Refs 54 and 55 are ca. 1 cm⁻¹ and 3 cm⁻¹, respectively. While the

TABLE I. Employed distance transformation parameters and polynomial degrees in the final fitting function

Polynomial	degree	a [bohr]
main (6-body)	7	1.9
extra 2-body	2	2.5
extra 3-body	3	1.7
extra 4-body	4	3.0

RMS weighted fitting error of PES25 is considerably better at 17.3 cm^{-1} , that is still an order of magnitude larger than the errors of the aforementioned PESs. This is attributable to a multitude of factors.

TABLE II. Assessment of PES25: number of geometries, root-mean-square error (RMSE) of the fitting set, for energy ranges relative to the *ab initio* equilibrium energy. The total RMSE and the RMS weighted error (RMSWE) over all geometry points are also listed.

Energy range [cm^{-1}]	# of geometries	RMSE [cm^{-1}]
0–13011	29029	13.8
13011–21947	7587	36.9
21947–43894	2785	69.8
Total points	39401	
Total RMSE		27.3
Total RMSWE		17.3

First, it is generally perilous to judge the quality of a statistical model (such as a fitted PES) only from its error over its fitting set, as the accuracy of the model can be vastly different at different geometries. This is illustrated by the fact that over the course of developing this PES we have accumulated over 174 000 geometries which were not included in the fit due to their weighted fitting error being less than 17.5 cm^{-1} . While this is still not a statistically independent test set, it does imply that the PES works well even for geometries not included in the fitting set.

Second, there are matters of geometry generation. The $\text{CH}_4\text{-Ar}$ PES in Ref. 54 was developed before the development of ROBOSURFER, and its fitting set was generated through the random distortion of methane’s equilibrium geometry, while the C–Ar distance and CH_4 orientation were randomly sampled. Since this was done without any steps to filter out geometries that would have already been well-described by the PES without them, it is likely that the RMS fitting error of the fitting set of Ref. 54 benefited from the sampling method. While the PES reported in Ref. 55 was developed with ROBOSURFER, PES25 is the result of far more sampling effort, which almost always raises the RMS errors of the fitting set, as it discovers and adds points of high error into the fit.

Third, the weighting function (Eq. S3 in the Supplementary Material) used for PES25 to fit the surface and select the geometries places much more importance on moderately high-energy geometries than the two previous PESs. As an example, while the development of PES25 considered all geometries up to $13\,011 \text{ cm}^{-1}$ equally important (a reasonable guess for a PES intended to describe vibrations up to $\text{ZPVE} + 2200 \text{ cm}^{-1}$), the weighting used in Ref. 55 would have only given a geometry at $13\,011 \text{ cm}^{-1}$ a weight of ~ 0.4 . As a result of this increased region of interest (in terms of energy), achieving a low RMS fitting error becomes much more challenging and demands more flexibility from the fitting function. And finally, of course, different molecular systems can be more or less challenging to create a PES for. It is possible that methanol is inherently a more difficult system to fit than $\text{CH}_4\text{-Ar}$ or $\text{CH}_4\text{-F}^-$.

The quality and improvement of PES25 over PES13 can also be assessed by comparing the *ab initio* computations and the literature values of Ref. 59. The molecular structure parameters are listed in Table III. The PES25 values agree well with the *ab initio* values with a maximum deviation of $3 \times 10^{-4} \text{ \AA}$ for bond lengths and 0.09° for bond angles. The largest changes are due to the different basis set, $2 \times 10^{-3} \text{ \AA}$ for bond lengths and 0.4° for bond angles (Table III, *ab initio* data). The accuracy of the PES fitting is sufficient to reflect the improvement in terms of the basis set size.

The harmonic frequencies and deviations from the *ab initio* computations are summarised in

TABLE III. Geometries at one of the three permutationally equivalent equilibrium structures and one saddle point obtained with PES13⁵⁹ and PES25 (this work) and *ab initio* computations. Bond lengths are in Å, bond angles are in degrees. The internal coordinates r , θ , and τ are defined in Fig. 1.

	Equilibrium structure				Saddle point			
	this work		Ref. 59		this work		Ref. 59	
	PES25	<i>ab initio</i> ^a	PES13	<i>ab initio</i> ^b	PES25	<i>ab initio</i> ^a	PES13	<i>ab initio</i> ^b
$r_1(\text{CO})$	1.4196	1.4199	1.419	1.422	1.4236	1.4235	1.423	1.423
$r_2(\text{OH})$	0.9583	0.9582	0.959	0.959	0.9558	0.9559	0.957	0.956
$r_3(\text{CH}_1)$	1.0876	1.0875	1.089	1.088	1.0908	1.0909	1.094	1.093
$r_{4,5}(\text{CH}_n, n = 2, 3)$	1.0931	1.0931	1.095	1.095	1.0909	1.0907	1.093	1.093
$\theta_1(\text{HOC})$	108.19	108.20	108.3	108.6	108.68	108.65	109.1	108.7
$\theta_2(\text{OCH}_1)$	106.65	106.74	106.7	106.8	112.05	112.04	112.7	112.1
$\theta_{3,4}(\text{OCH}_n, n = 2, 3)$	111.94	111.90	111.9	112.0	109.50	109.49	109.4	109.5
$\tau_1(\text{H}_1\text{COH})$	180.00	180.00	180.0	180.0	0.00	0.00		
$\tau_2(\text{H}_2\text{COH})$	61.39	61.39			-120.37	-120.39		
$\tau_3(\text{H}_3\text{COH})$	298.61	298.61			120.37	120.39		

^a CCSD(T)-F12b/cc-pVTZ-F12 ^b CCSD(T)-F12b/aug-cc-pVDZ

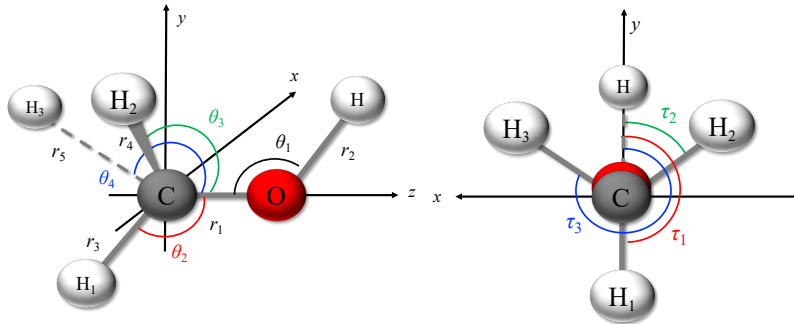


FIG. 1. Definition of the primitive internal coordinates of the methanol molecule and the body-fixed Cartesian frame used in this work.

Table IV. Both MAE and MAX errors of PES25 are less than those of Ref. 59. Most of the harmonic frequencies obtained with the two *ab initio* computations agree within a few cm^{-1} , and the largest deviation of more than 6.0 cm^{-1} is found for the modes related to the H-O-C-H_n ($n = 1, 2, 3$) dihedral angles. Interestingly, the torsional harmonic frequency changes by more than 10 cm^{-1} by changing from PES13 to PES25. However, most of the variational vibrational energies corresponding to the torsional motion are less sensitive to this change (Table S7 of the Supplementary Material). The largest deviation, 8.3 cm^{-1} , is observed in the 1800 cm^{-1} region beyond the ZPVE (Table S8 of the Supplementary Material).

As a final test of the quality of PES25, we have prepared one-dimensional slices of the PES along selected internal coordinates, which extend into regions moderately far from the equilibrium structure. As shown in Figs. S11–S13 of the Supplementary Material, the fitting errors along these slices match the RMS weighted fitting error of the fitting set.

III. VARIATIONAL VIBRATIONAL COMPUTATIONS

A. Methodological details

We solve the vibrational Schrödinger equation,

$$[\hat{T}^v + V]\Psi_n = E_n\Psi_n \quad (3)$$

TABLE IV. Harmonic frequencies and harmonic zero-point vibrational energy (ZPVE) in cm^{-1} at one of the three permutationally equivalent equilibrium structures and one saddle point obtained with the PES25 and *ab initio* computations. The harmonic frequencies of Ref. 59 are listed in decreasing energetic order. Mean absolute errors (MAE) and maximum (MAX) errors of the harmonic frequencies computed with the PESs and obtained from the *ab initio* computations are also shown.

description	coord	sym	Equilibrium structure				Saddle point			
			this work		Ref. 59		this work		Ref. 59	
			PES25	<i>ab initio</i> ^a	PES13	<i>ab initio</i> ^b	PES25	<i>ab initio</i> ^a	PES13	<i>ab initio</i> ^b
$\nu(\text{OH})$	r_{OH}	a'	3863.1	3866.4	3869.5	3864.9	3898.5	3900.5	3901.8	3901.5
$\nu(\text{CH}_3)_{\text{asym}}$	r_{CH}	a'	3134.4	3136.7	3150.3	3133.0	3104.9	3107.9	3120.8	3106.1
$\nu(\text{CH}_3)_{\text{asym}}$	r_{CH}	a''	3073.1	3075.7	3068.8	3071.9	3093.8	3101.9	3090.2	3100.5
$\nu(\text{CH}_3)_{\text{sym}}$	r_{CH}	a'	3014.6	3015.9	3016.2	3013.4	3026.0	3029.1	3018.4	3029.6
$\delta(\text{CH}_3)_{\text{asym}}$	φ_2	a'	1525.0	1521.6	1527.1	1514.8	1528.2	1529.2	1518.4	1526.8
$\delta(\text{CH}_3)_{\text{asym}}$	φ_1	a''	1512.4	1511.1	1499.0	1504.6	1505.7	1500.8	1508.6	1499.2
$\delta(\text{CH}_3)_{\text{sym}}$	θ_{HCO}	a'	1485.4	1485.4	1476.0	1481.3	1487.9	1489.5	1498.2	1487.7
$\delta(\text{COH})$	θ_{COH}	a'	1378.8	1383.7	1376.8	1380.5	1355.9	1366.1	1369.0	1366.0
$\rho(\text{CH}_3)$	θ_{HCO}	a''	1177.7	1181.7	1196.2	1178.4	1186.6	1191.5	1191.4	1192.3
$\rho(\text{CH}_3)$	θ_{HCO}	a'	1091.9	1090.1	1067.0	1089.5	1097.5	1096.7	1080.3	1100.3
$\nu(\text{CO})$	r_{CO}	a'	1063.3	1062.2	1065.2	1064.3	1062.2	1063.1	1058.5	1069.1
tor(OH)	τ	a''	298.7	293.1	287.0	289.2	300.2 <i>i</i>	296.8 <i>i</i>	301.9 <i>i</i>	284.8 <i>i</i>
ZPVE			11309.5	11311.8	11299.6	11292.9	11173.8	11188.1	11177.8	11189.6
MAE			2.6		8.2		3.6		9.7	
MAX			5.7		22.5		10.2		20.0	

^a CCSD(T)-F12b/cc-pVTZ-F12 ^b CCSD(T)-F12b/aug-cc-pVDZ

using the V potential energy surface developed in the first part of this work. The vibrational kinetic energy operator is

$$\hat{T}^v = -\frac{\hbar^2}{2} \sum_{k=1}^D \sum_{l=1}^D G_{kl} \frac{\partial}{\partial \rho_k} \frac{\partial}{\partial \rho_l} - \frac{\hbar^2}{2} \sum_{k=1}^D B_k \frac{\partial}{\partial \rho_k} + U \quad (4)$$

with

$$B_k = \sum_{l=1}^D \frac{\partial}{\partial \rho_l} G_{lk} \quad (5)$$

and

$$U = \frac{\hbar^2}{32} \sum_{k=1}^D \sum_{l=1}^D \left[\frac{G_{kl}}{\tilde{g}^2} \frac{\partial \tilde{g}}{\partial \rho_k} \frac{\partial \tilde{g}}{\partial \rho_l} + 4 \frac{\partial}{\partial \rho_k} \left(\frac{G_{kl}}{\tilde{g}} \frac{\partial \tilde{g}}{\partial \rho_l} \right) \right], \quad (6)$$

where D is the vibrational dimensionality (here $D = 12$), $\tilde{g} = \det \mathbf{g}$ is the determinant and $G_{kl} = (\mathbf{g}^{-1})_{kl}$ labels elements of the inverse of the mass-weighted metric tensor corresponding to the coordinate transformation from laboratory-frame Cartesian coordinates to rotational and internal, vibrational coordinates (the overall molecular translation is exactly separated⁴⁴).

The ρ_k internal coordinate definition is summarised as follows. To have a large-amplitude torsional coordinate that carries the permutation symmetry of the three hydrogens of the methyl unit, we define the following linear combinations of the τ_1, τ_2 and τ_3 primitive dihedral angles

(Fig. 1)^{50,76,77},

$$\tau = \frac{1}{3} (\tau_1 + \tau_2 + \tau_3), \quad (7)$$

$$\varphi_1 = \frac{1}{\sqrt{2}} (\tau_2 - \tau_3), \quad (8)$$

$$\varphi_2 = \frac{1}{\sqrt{6}} (2\tau_1 - \tau_2 - \tau_3). \quad (9)$$

The dynamically relevant interval for τ is $[0, 2\pi)$; φ_1 and φ_2 are small-amplitude coordinates. To describe the small-amplitude vibrations, we start with the bond distances and angles of the valence coordinates (Fig. 1) and add φ_1 and φ_2 of Eqs. (8)–(9),

$$\boldsymbol{\xi} = (r_1, r_2, r_3, r_4, r_5, \theta_1, \theta_2, \theta_3, \theta_4, \varphi_1, \varphi_2). \quad (10)$$

Then, we define the q_k curvilinear normal coordinates by the linear combination of the $D^s = 11$ small-amplitude coordinates as

$$\Delta\xi_i = \sum_{k=1}^{D^s} L_{ik} q_k \quad \text{with} \quad \Delta\xi_i = \xi_i - \xi_i^{\text{ref}}(\tau), \quad i = 1, \dots, D^s. \quad (11)$$

$\boldsymbol{\xi}^{\text{ref}}(\tau)$ is the minimum-energy path on the PES for τ . \mathbf{L} diagonalizes the $\bar{\mathbf{G}}^s \bar{\mathbf{F}}^s$ matrix, where $\bar{\mathbf{G}}^s$ and $\bar{\mathbf{F}}^s$ are obtained by averaging the elements of the $D^s \times D^s$ $\mathbf{G}^s(\tau_i)$ matrix and the $\mathbf{F}^s(\tau_i)$, the second derivative matrix of the potential energy function, over the three minimum structures, $\tau_i = \pi/3, \pi, 5\pi/3$. Eq. 11 defines the small-amplitude q_k coordinates, and so, the vibrational coordinates used in the vibrational kinetic energy operator, Eq. (4), are $\boldsymbol{\rho} = (q_1, \dots, q_{D^s}; \tau)$. As a result of this construction, the coupling of the small-amplitude coordinates is small (at the harmonic level), and thus, we can use an efficient basis and grid pruning. Further details (and possible coordinate choices) are described in Ref. 58. We note that the $\boldsymbol{\xi}^{\text{ref}}(\tau)$ minimum-energy path and the \mathbf{L} coefficients were (re-)computed with the PES25 developed in the first part of this work, the associated harmonic frequencies are provided in the Supplementary Material (Table S6).

TABLE V. Deviation of the vibrational band origins, $\tilde{\nu}$ in cm^{-1} , of CH_3OH computed with the GENIUSH-Smolyak program with PES13⁵⁹ and PES25 (this work) from available experimental data.

Description	Energy range [cm^{-1}]	$\tilde{\nu}$ (PES13) ⁵⁸			$\tilde{\nu}$ (PES25)		
		MAE	RMSE	MAX	MAE	RMSE	MAX
(a) torsional excitations:	0–1050	1.6	1.9	3.2	0.9	1.1	2.1
(b) SAM-torsion couplings:	1050–2000	6.9	8.4	16.1	1.5	2.0	4.0
(c) combination bands:	2000–2200	9.3	11.9	21.3	1.5	1.8	3.2

We solve Eq. (3) in a variational procedure; harmonic oscillator basis functions are used for the q_k small-amplitude degrees of freedom, and Fourier basis functions for the τ large-amplitude degree of freedom. A direct product basis representation would be too large for this 12D system, so we exploit that the coupling of the small-amplitude vibrations is small^{44,56–58} and we can truncate the direct-product basis. For the computation of the Hamiltonian matrix, we use the Smolyak non-product grid to numerically compute integrals for the small-amplitude coordinates^{52–54,57,78,79}. The \mathbf{g} matrix and all further kinetic energy coefficients are computed over the multi-dimensional grid of the vibrational coordinates (q_k and τ) and the t -vector formalism is used as described in Refs. 44,80 and 52. Regarding the number of basis functions and grid points, extensive convergence tests on PES13 have been reported in Ref. 58. In this work, the following basis and grid parameters are used in the GENIUSH-Smolyak computation (the definition of these computational parameters can be found in Refs. 52,53,56–58): $n_\tau = 32$ and $M_\tau = 54$ for the LAM basis and grid size; and $b = 7$ and $H = 21$ for the SAM basis truncation and grid pruning which converge the vibrational energies within 0.5 cm^{-1} up to 2000 cm^{-1} from the ZPVE and within 1.5 cm^{-1} up to 2200 cm^{-1} .

B. Vibrational energies

First of all, we compare the vibrational energies computed with the newly developed PES25, and with the previously available PES13⁵⁹. For the comparison, we match the vibrational states based on their assignment, and this assignment also helps us compare with data from (gas-phase) experiment. The vibrational energies and assignments with PES13 are taken from Ref. 58, and the new, detailed assignments with PES25 are collected in Tables S7-S9 of the Supplementary Material. The mean absolute error (MAE), root mean square error (RMSE), and maximum error (MAX) resulting from this analysis are shown in Table V.

The comparison, in Table V, is shown over three energy ranges defined according to the vibrational excitation types: (a) torsional states, 0–1050 cm^{-1} ; (b) vibration-torsion coupling states, 1050–1600 cm^{-1} ; and (c) combination bands, 2000–2200 cm^{-1} . To prepare Table V, only gas-phase experimental data were used. There are further, matrix-isolation vibrational band origins in neon and nitrogen matrices available in the literature. They are included in Table S9 of the Supplementary Material, and the agreement is mostly good with our variational results. However, direct, quantitative comparison (as for gas-phase data) is hindered by unpredictable matrix effects, which may be larger than the inaccuracy of our computations.

We also report that while the computed and experimental vibrational band origins (VBOs) are within a few cm^{-1} with PES13 or PES25 for the lowest-energy (a) range; the RMSE (MAX) of the VBOs increases to 12 (21) cm^{-1} for PES13 for the combination band range (c). At the same time, for the newly developed PES25, the RMSE (MAX) of the VBOs remains small, and even for the high-energy (c) range, it is only 1.8 (3.2) cm^{-1} , far lower than the RMS fitting errors of the fitting set of PES25.

The computed VBOs using PES25 and the deviation from the available experiments are listed in Table VI.

There are several VBOs, for which there is currently no (gas-phase) experimental value available. For an overall assessment, we compare the VBOs of the PES13 and PES25 in Figure 2, which reveals large, $> 10 \text{ cm}^{-1}$, deviations beyond ca. 1500 cm^{-1} . The figure also shows the deviations from the gas-phase experimental data summarised in Table V.

These observations suggest that PES25 represents a major improvement over earlier PES representations and provides a (near) spectroscopic quality description not only for the torsional excitation range but also for the vibration-torsion coupling and combination bands.

At this point, it is appropriate to consider the major sources of remaining errors due to approximations and missing physical corrections. This short analysis may guide future improvements and set expected uncertainties for numerical applications. First of all, the current PES relies on frozen-core electronic energies computed at the CCSD(T) level, and it has been known that the correlation effects of core electrons largely cancel the high-order correlation effects beyond CCSD(T)^{81,82}. Any future improvement will require improvement of both aspects. At the same time, the core-electron correlation effects have been reported to be important for accurate rotational constants (affecting them at the level of hundreds of MHz^{83,84}). Hence, corrections will be considered for an accurate description of the rotational-vibrational spectrum.

Furthermore, the present work uses a triple-zeta electronic basis set. It was noted in Ref. 85 that the harmonic oscillator wave numbers' (finite basis set) error can be reduced by ca. 50 % upon enlarging the electronic basis set to quadruple-zeta quality [from 1.7 cm^{-1} (cc-pVTZ-F12) to 0.8 cm^{-1} (cc-pVQZ-F12) root mean square error in that particular study]. A comparable improvement is anticipated for a fully-coupled anharmonic treatment.

An additional source of error in the vibrational energies originates from the fitting error of the PES, which was already discussed in detail in Sec. II (and in the Supplementary Material).

Further small errors are due to missing finite-nuclear mass corrections, *i.e.*, the diagonal Born-Oppenheimer correction and the (less known) effective rotational-vibrational masses (in the present work, we used atomic masses). Relativistic and quantum-electrodynamical effects will also be relevant when the electronic structure representation is substantially improved. These small physical effects are often neglected in a standard electronic structure computation, but have been of interest in the spectroscopy community^{86–88}. Rigorous information on their contributions is available from recent studies of few-electron diatomic molecules^{89–93}.

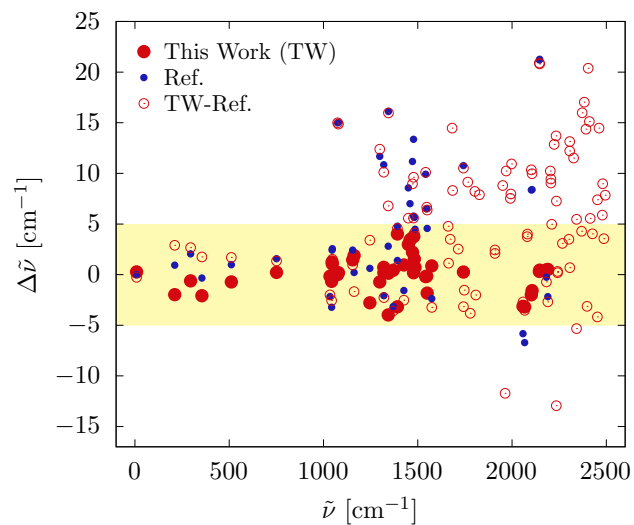


FIG. 2. Variational vibrational band origins computed in this work, with the newly developed PES25, at the CCSD(T)-F12b/cc-pVTZ-F12 level of electronic structure theory and the GENIUSH-Smolyak program, reproduce experimental data with $\Delta\tilde{\nu}$ difference less than $\pm 5 \text{ cm}^{-1}$. They significantly improve upon earlier results (Ref.) computed with PES13⁵⁹ and reported in Ref. 58. The vibrational band origins are referenced to the ZPVE of each computation. The ZPVEs with the PES13 and the PES25 are 11108.0 cm^{-1} ¹⁵⁸ and 11119.6 cm^{-1} (this work).

TABLE VI. Variational vibrational energies, $\tilde{\nu}$ in cm^{-1} , referenced to the zero-point vibrational energy (ZPVE, 11119.6 cm^{-1}) of CH_3OH in 12D computed with the GENIUSH-Smolayk program ($b = 7$ basis set) and PES25 developed in the present work.

#	ν_τ^a	SAMs ^b	Γ^c	$\tilde{\nu}$	δ^d	#	ν_τ^a	SAMs ^b	Γ^c	$\tilde{\nu}$	δ^d	#	ν_τ^a	SAMs ^b	Γ^c	$\tilde{\nu}$
1	0	0	A_1	0		51-52	2	8_1	E	1549.9	[-1.8]	103-104	3	5_1	E	2203.0
2-3	0	0	E	8.9	[0.3]	53-54	1	6_1	E	1574.5	[0.9]	105	3	$4_1, 10_1$	A_2	2205.8
4-5	1	0	E	210.9	[-2.0]	55-56	1,2	$5_1, 7_1, 11_1$	E	1661.1		106	3	$4_1, 10_1$	A_1	2206.2
6	1	0	A_2	295.1	[-0.6]	57-58	1	5_1	E	1663.9		107-108	3,4	$7_1, 11_1$	E	2210.4
7	2	0	A_1	355.3	[-2.1]	59	1	$4_1, 10_1$	A_2	1672.2		109-110	0	$7_2, 11_2$	E	2223.8
8-9	2	0	E	511.0	[-0.7]	60	1	$4_1, 10_1$	A_1	1682.5		111	0,1	mix	A_2	2233.7
10-11	3	0	E	750.8	[0.2]	61-62	1	$4_1, 10_1$	E	1685.0		112-113	3,4	$7_1, 11_1$	E	2234.6
12	0	8_1	A_1	1034.5	[-0.2]	63	1,2	$6_1, 7_1, 11_1$	A_2	1714.7		114-115	3	$4_1, 10_1$	E	2235.1
13-14	0	8_1	E	1043.3	[-0.7]	64	2	$6_1, 7_1, 11_1$	A_1	1742.2		116	5	0	A_2	2241.4
15	3	0	A_2	1045.4	[1.2]	65-66	2	6_1	E	1742.4	[0.3]	117	6	0	A_1	2241.5
16	4	0	A_1	1046.5	[1.1]	67	1	5_1	A_2	1746.6		118-119	1	8_2	E	2267.5
17	0	$6_1, 7_1, 11_1$	A_1	1074.7	[0.0]	68-69	1	$4_1, 10_1$	E	1765.1		120	0	mix	A_1	2301.6
18-19	0	$6_1, 7_1, 11_1$	E	1079.1	[0.2]	70-71	3	8_1	E	1778.5		121	4	6_1	A_1	2306.2
20-21	0	$7_1, 11_1$	E	1155.0	[1.5]	72-73	5	0	E	1803.0		122	3	6_1	A_2	2306.2
22	0	$7_1, 11_1$	A_2	1162.1	[1.9]	74	2	5_1	A_1	1807.7		123-124	0	mix	E	2306.3
23-24	1	8_1	E	1245.8	[-2.8]	75-76	2	$4_1, 10_1$	E	1827.1		125-126	0	mix	E	2326.3
25-26	0	6_1	E	1298.2	[-0.7]	77	3	$7_1, 11_1$	A_1	1909.7		127	1	8_2	A_2	2342.2
27	0,1	$6_1, 7_1, 11_1$	A_1	1319.9	[0.7]	78	3	$7_1, 11_1$	A_2	1909.8		128	0	mix	A_1	2342.3
28	1	$7_1, 8_1, 11_1$	A_2	1320.4	[0.2]	79-80	2,3	$6_1, 7_1, 11_1$	E	1950.9		129-130	1	mix	E	2368.8
29-30	1	6_1	E	1343.5	[-4.0]	81-82	2	5_1	E	1963.1		131	1	8_2	A_2	2372.0
31	1	8_1	A_2	1344.9	[0.1]	83-84	2	$4_1, 10_1$	E	1969.1		132	0	6_2	A_1	2383.6
32	0,2	$6_1, 7_1, 11_1$	A_1	1369.3	[0.4]	85	2	$4_1, 10_1$	A_2	1991.2		133-134	0,1	$6_2, 7_2, 11_2$	E	2392.3
33	2	8_1	A_1	1392.1	[-3.2]	86	2	$4_1, 10_1$	A_1	1993.8		135	0	mix	A_1	2397.9
34-35	4	0	E	1392.2	[4.0]	87-88	3	6_1	E	1997.5		136	0	mix	A_2	2403.9
36-37	1	$7_1, 11_1$	E	1426.2	[1.0]	89	0	8_2	A_1	2058.1	[-3.1]	137-138	0,1	$6_2, 7_2, 11_2$	E	2410.4
38	0	5_1	A_1	1450.3	[3.0]	90-91	0	8_2	E	2066.8	[-3.2]	139	2	8_2	A_1	2414.9
39-40	0	5_1	E	1458.7	[3.4]	92	3	8_1	A_2	2080.9		140-141	4	8_1	E	2426.6
41-42	0	$4_1, 10_1$	E	1471.7	[2.2]	93	4	8_1	A_1	2081.9		142-143	1	mix	E	2452.6
43-44	2	$7_1, 11_1$	E	1477.4		94	0	mix	A_1	2102.2	[-2.0]	144	1	mix	A_1	2453.4
45	0	$4_1, 10_1$	A_2	1477.8	[3.7]	95-96	0	mix	E	2106.4	[-1.6]	145-146	0	mix	E	2461.5
46-47	0	$4_1, 10_1$	E	1481.8	[1.5]	97	0	mix	A_1	2144.8	[0.3]	147	0	$5_1 + 8_1$	A_1	2478.9
48	0	$4_1, 10_1$	A_1	1485.4	[0.7]	98-99	0	mix	E	2146.9	[0.4]	148	0,1	mix	A_2	2481.0
49	1	6_1	A_2	1541.7	[-0.2]	100-101	0	mix	E	2182.5	[0.5]	149	0	$5_1 + 8_1$	E	2487.2
50	2	6_1	A_1	1547.4	[-0.1]	102	0	mix	A_2	2190.1	[0.5]	150	0,2	mix	E	2494.3

^a Assignment of the torsional excitation similarly to Ref. 58.

^b Assignment in terms of the (small-amplitude, SAM) curvilinear normal modes $1_n, 2_n, \dots, 11_n$ ($n = 0, 1, \dots$). Zero excitation ($n = 0$) is noted as '0'. The label 'Mix' stands for strongly mixed states.

^c Γ : $C_{3v}(M)$ irreducible representation label. Further details are described in Sec. S1 of the Supporting Information of Ref. 58.

^d Deviation from the experimental vibrational band origin^{19,22-24,94,95}, $\delta = \tilde{\nu}_{\text{exp}} - \tilde{\nu}$ in cm^{-1} . Gas-phase experimental data were not available to us for the states #103-150. Matrix-isolation data are cited in Table S9 of the Supplementary Material.

IV. SUMMARY, CONCLUSION, AND OUTLOOK

We have reported the development of an *ab initio* potential energy surface and variational vibrational states for the methanol molecule.

The electronic structure computations were carried out at the CCSD(T)-F12b/cc-pVTZ-F12 level of theory, the dataset for the PES was generated with the ROBOSURFER code, and the PES was fitted using the permutationally invariant polynomials (PIP) method. Properties of the PES, including molecular structure parameters, harmonic frequencies, and one-dimensional slices, were thoroughly investigated, and all details reproduce the *ab initio* values well.

The vibrational states of methanol were computed using this newly developed PES and the GENIUSH-Smolyak approach up to the coupling between the torsion and the overtone of the C-O stretching vibration (ca. 2500 cm^{-1} beyond the zero-point vibrational energy). The resulting vibrational band origins improve upon, by $10\text{-}20\text{ cm}^{-1}$, earlier vibrational results (computed on PES13) and are in good agreement ($\pm 5\text{ cm}^{-1}$) with available gas-phase experimental data. In the variational vibrational computations, we have confirmed that the vibrational energies are converged within $1\text{-}2\text{ cm}^{-1}$ with respect to the vibrational basis for these ranges.

As a result, we describe the quantum dynamics of methanol here using a fully *ab initio* approach, confirmed with experiment from the torsional excitation range, through the vibration-torsion coupling, up to the start of the combination bands range at around 2500 cm^{-1} beyond the zero-point vibrational energy. This result opens the door for future rovibrational computations, for which we plan to implement a path-following, body-fixed frame approach. Furthermore, the development of electric dipole and polarizability surfaces is in progress. This will allow us a fully *ab initio* computation and line-by-line study of the high-resolution infrared and Raman spectra of methanol. All in all, the present work is an important step towards simulating the ‘complete’ rovibrational spectrum of methanol (and isotopologues) for further applications in astrochemistry, astrophysics, and fundamental physics.

ACKNOWLEDGMENTS

AS thanks the European Union’s Horizon 2022 research and innovation programme for funding under the Marie Skłodowska-Curie Grant Agreement No. 101105452 (QDMAP). AS and EM thank the financial support of the Hungarian National Research, Development, and Innovation Office (FK 142869). TG and GC thank the National Research, Development and Innovation Office-NKFIH, K-146759; project no. TKP2021-NVA-19, provided by the Ministry of Culture and Innovation of Hungary from the National Research, Development and Innovation Fund, financed under the TKP2021-NVA funding scheme; and the Momentum (Lendület) Program of the Hungarian Academy of Sciences for financial support. We acknowledge KIFÜ (Governmental Agency for IT Development, Hungary) for awarding us access to the Komondor HPC facility based in Hungary. We thank Viktor Tajti (Szeged) for the extension of the QCT MD code to compute unimolecular trajectories.

-
- [1] P. Jansen, L.-H. Xu, I. Kleiner, W. Ubachs, and H. L. Bethlem, Methanol as a sensitive probe for spatial and temporal variations of the proton-to-electron mass ratio, *Phys. Rev. Lett.* **106**, 100801 (2011).
 - [2] S. A. Levshakov, M. G. Kozlov, and D. Reimers, Methanol as a tracer of fundamental constants, *ApJ* **738**, 26 (2011).
 - [3] J. Bagdonaite, P. Jansen, C. Henkel, H. Bethlem, K. Menten, and W. Ubachs, A stringent limit on a drifting proton-to-electron mass ratio from alcohol in the early universe, *Science* **339**, 46 (2013).
 - [4] J. S. Vorotyntseva, M. G. Kozlov, and S. A. Levshakov, Methanol isotopologues as a probe for spatial and temporal variations of the electron-to-proton mass ratio, *Mon. Not. R. Astron. Soc.* **527**, 2750 (2023).
 - [5] A. Sunaga, Strong parity-violation effects induced by large-amplitude motions: A quantum-dynamics study of substituted chiral methanols, *J. Chem. Phys.* **162**, 064302 (2025).
 - [6] B. Lankhaar, W. Vlemmings, G. Surcis, H. J. van Langevelde, G. C. Groenenboom, and A. van der

- Avoird, Characterization of methanol as a magnetic field tracer in star-forming regions, *Nat. Astron.* **2**, 145 (2018).
- [7] I. Kleiner, Spectroscopy of interstellar internal rotors: An important tool for investigating interstellar chemistry, *ACS Earth Space Chem.* **3**, 1812 (2019).
 - [8] J. K. Jørgensen, M. H. D. van der Wiel, A. Coutens, J. M. Lykke, H. S. P. Müller, E. F. van Dishoeck, H. Calcutt, P. Bjerkeli, T. L. Bourke, M. N. Drozdovskaya, C. Favre, E. C. Fayolle, R. T. Garrod, S. K. Jacobsen, K. I. Öberg, M. V. Persson, and S. F. Wampfler, The ALMA protostellar interferometric line survey (PILS): First results from an unbiased submillimeter wavelength line survey of the class 0 protostellar binary IRAS 16293-2422 with ALMA, *Astron. Astrophys.* **595**, A117 (2016).
 - [9] T. Oyama, Y. Ohno, A. Tamanai, Y. Watanabe, S. Yamamoto, T. Sakai, S. Zeng, R. Nakatani, and N. Sakai, Laboratory measurement of CH₂DOH line intensities in the millimeter-wave region, *Astrophys. J.* **957**, 4 (2023).
 - [10] W. Riedel, O. Sipilä, E. Redaelli, P. Caselli, A. I. Vasyunin, F. Dulieu, and N. Watanabe, Modelling deuterated isotopologues of methanol towards the pre-stellar core L1544, *Astron. Astrophys.* **680**, A87 (2023).
 - [11] J.-H. Jeong, J.-E. Lee, S. Lee, G. Baek, J.-H. Kang, S. Lee, C.-H. Kim, H.-S. Yun, Y. Aikawa, G. J. Herczeg, D. Johnstone, and L. Cieza, ALMA spectral survey of an eruptive young star, V883 ori (ASSAY). II. freshly sublimated complex organic molecules in the keplerian disk, *Astrophys. J. Suppl. Ser.* **276**, 49 (2025).
 - [12] A. Tamanai, T. Oyama, Y. Watanabe, T. Sakai, R. Nakatani, S. Zeng, I. Kleiner, and N. Sakai, Laboratory measurement of CH₃¹⁷OH transitions in the frequency range from 216 to 264 GHz for astronomical application, *Astrophys. J.* **980**, 110 (2025).
 - [13] A. Borden and E. F. Barker, The infra-red absorption spectrum of methyl alcohol, *J. Chem. Phys.* **6**, 553 (1938).
 - [14] J. O. Halford, L. C. Anderson, and G. H. Kissin, The raman spectra of the methyl alcohols, CH₃OH, CH₃OD, and CH₂DOD, *J. Chem. Phys.* **5**, 927 (1937).
 - [15] C. Tanaka, K. Kuratani, and S.-I. Mizushima, In-plane normal vibrations of methanol, *Spectrochim. Acta* **9**, 265 (1957).
 - [16] M. Falk and E. Whalley, Infrared spectra of methanol and deuterated methanols in gas, liquid, and solid phases, *J. Chem. Phys.* **34**, 1554 (1961).
 - [17] A. Timidei and G. Zerbi, Valence force constants and normal vibrations of methanol, *Z. Naturforsch. A* **25**, 1729 (1970).
 - [18] T. Shimanouchi, *Tables of Molecular Vibrational Frequencies Consolidated, vol. 1* (Nat. Stand. Ref. Data Ser., Nat. Bur. Stand. (U.S.), 1972).
 - [19] A. Serrallach, R. Meyer, and H. Günthard, Methanol and deuterated species: Infrared data, valence force field, rotamers, and conformation, *J. Mol. Spectrosc.* **52**, 94 (1974).
 - [20] E. Herbst, J. K. Messer, and F. C. de Lucia, A new analysis and additional measurements of the millimeter and submillimeter spectrum of methanol, *J. Mol. Spectrosc.* **108**, 42 (1984).
 - [21] L.-H. Xu, M. S. Walsh, and R. M. Lees, Global fit of torsion – rotation transitions in the ground and first excited torsional states of ¹³C-Methanol, *J. Mol. Spectrosc.* **179**, 269 (1996).
 - [22] R. M. Lees, M. Mollabashi, L.-H. Xu, M. Lock, and B. P. Winnewisser, Variations in the torsion-vibration energy structure of CH₃OH from fundamental, overtone, and combination bands of the ν_7, ν_8 and ν_{11} CH₃ rocking and CO stretching modes, *Phys. Rev. A* **65**, 042511 (2002).
 - [23] R. M. Lees, L.-H. Xu, J. W. C. Johns, Z.-F. Lu, B. P. Winnewisser, M. Lock, and R. L. Sams, Fourier transform spectroscopy of CH₃OH: rotation–torsion–vibration structure for the CH₃-rocking and OH-bending modes, *J. Mol. Spectrosc.* **228**, 528 (2004).
 - [24] M. Abouti Tamsamani, L.-H. Xu, and R. M. Lees, A rotation–torsion–vibration treatment with three-dimensional internal coordinate approach and additional FTIR spectral assignments for the CH₃-bending fundamentals of methanol, *J. Mol. Spectrosc.* **218**, 220 (2003).
 - [25] L.-H. Xu, J. Fisher, R. M. Lees, H. Y. Shi, J. T. Hougen, J. C. Pearson, B. J. Drouin, G. A. Blake, and R. Braakman, Torsion–rotation global analysis of the first three torsional states ($\nu_t = 0, 1, 2$) and terahertz database for methanol, *J. Mol. Spectrosc.* **251**, 305 (2008).
 - [26] R. Santagata, D. B. A. Tran, B. Argence, O. Lopez, S. K. Tokunaga, F. Wiotte, H. Mouhamad, A. Goncharov, M. Abgrall, Y. Le Coq, H. Alvarez-Martinez, R. Le Targat, W. K. Lee, D. Xu, P.-E. Pottie, B. Darquié, and A. Amy-Klein, High-precision methanol spectroscopy with a widely tunable SI-traceable frequency-comb-based mid-infrared QCL, *Optica* **6**, 411 (2019).
 - [27] P. R. Bunker and P. Jensen, *Molecular Symmetry and Spectroscopy, 2nd Ed* (NRC Research Press, 2006).
 - [28] M. Quack, Detailed symmetry selection rules for reactive collisions, *Mol. Phys.* **34**, 477 (1977).
 - [29] M. Quack and F. Merkt, *Handbook of High-resolution Spectroscopy* (John Wiley & Sons, 2011).
 - [30] J. P. Perchard, The torsion-vibration spectrum of methanol trapped in neon matrix, *Chem. Phys.* **332**, 86 (2007).
 - [31] J. P. Perchard, F. Romain, and Y. Bouteiller, Determination of vibrational parameters of methanol from matrix-isolation infrared spectroscopy and ab initio calculations. part 1 – spectral analysis in

- the domain 11000–200 cm^{-1} , *Chem. Phys.* **343**, 35 (2008).
- [32] D. F. Dinu, K. Oenen, J. Schlagin, M. Podewitz, H. Grothe, T. Loerting, and K. R. Liedl, How vibrational notations can spoil infrared spectroscopy: A case study on isolated methanol, *ACS Phys. Chem. Au* **4**, 679 (2024).
- [33] J. M. Bowman, Self-consistent field energies and wavefunctions for coupled oscillators, *J. Chem. Phys.* **68**, 608 (1978).
- [34] K. Yagi, K. Hirao, T. Taketsugu, M. W. Schmidt, and M. S. Gordon, Ab initio vibrational state calculations with a quartic force field: applications to H_2CO , C_2H_4 , CH_3OH , CH_3CCH , and C_6H_6 , *J. Chem. Phys.* **121**, 1383 (2004).
- [35] F. Partal Ureña, J. J. López González, and F. Márquez, Anharmonic spectra of methanol and silanol: A comparative study, *J. Mol. Spectrosc.* **233**, 203 (2005).
- [36] Y. Scribano, D. M. Lauvergnat, and D. M. Benoit, Fast vibrational configuration interaction using generalized curvilinear coordinates and self-consistent basis, *J. Chem. Phys.* **133**, 094103 (2010).
- [37] B. Schröder and G. Rauhut, Vibrational configuration interaction theory, in *Vibrational Dynamics of Molecules* (WORLD SCIENTIFIC, 2022) pp. 1–40.
- [38] D. F. Dinu, M. Podewitz, H. Grothe, T. Loerting, and K. R. Liedl, On the synergy of matrix-isolation infrared spectroscopy and vibrational configuration interaction computations, *Theor. Chem. Acc.* **139**, 174 (2020).
- [39] H. R. Larsson, Benchmarking vibrational spectra: 5000 accurate eigenstates of acetonitrile using tree tensor network states, *J. Phys. Chem. Lett.* **16**, 3991 (2025).
- [40] A. G. Császár, C. Fábri, T. Szidarovszky, E. Mátyus, T. Furtenbacher, and G. Czakó, The fourth age of quantum chemistry: molecules in motion, *Phys. Chem. Chem. Phys.* **14**, 1085 (2012).
- [41] J. Tennyson, Perspective: Accurate ro-vibrational calculations on small molecules, *J. Chem. Phys.* **145**, 120901 (2016).
- [42] T. Carrington, Jr, Perspective: Computing (ro-)vibrational spectra of molecules with more than four atoms, *J. Chem. Phys.* **146**, 120902 (2017).
- [43] A. Chen, A. Nauts, and D. Lauvergnat, ElVibRot-MPI: parallel quantum dynamics with smolyak algorithm for general molecular simulation, *arXiv [physics.comp-ph]* (2021), [arXiv:2111.13655 \[physics.comp-ph\]](https://arxiv.org/abs/2111.13655).
- [44] E. Mátyus, A. Martín Santa Daría, and G. Avila, Exact quantum dynamics developments for floppy molecular systems and complexes, *Chem. Commun.* **59**, 366 (2023).
- [45] J. Simmons and T. Carrington, Jr, Computing vibrational spectra using a new collocation method with a pruned basis and more points than basis functions: Avoiding quadrature, *J. Chem. Phys.* **158**, 144115 (2023).
- [46] R. Wodraszka and T. Carrington, Jr, Using a pruned basis and a sparse collocation grid with more points than basis functions to do efficient and accurate MCTDH calculations with general potential energy surfaces, *J. Chem. Phys.* **160**, 214121 (2024).
- [47] S. D. Kallullathil and T. Carrington, Computing vibrational energy levels using a canonical polyadic tensor method with a fixed rank and a contraction tree, *J. Chem. Phys.* **158**, 214102 (2023).
- [48] I. Simkó, P. M. Felker, and Z. Bačić, HCl trimer: HCl-stretch excited intramolecular and intermolecular vibrational states from 12D fully coupled quantum calculations employing contracted intra- and inter-molecular bases, *J. Chem. Phys.* **160**, 164304 (2024).
- [49] I. Simkó, P. Felker, and Z. Bačić, H_2O trimer: Rigorous 12D quantum calculations of intermolecular vibrational states, tunneling splittings, and low-frequency spectrum, *J. Chem. Phys.* **162**, 034301 (2025).
- [50] D. Lauvergnat and A. Nauts, Quantum dynamics with sparse grids: a combination of smolyak scheme and cubature. application to methanol in full dimensionality, *Spectrochim. Acta A Mol. Biomol. Spectrosc.* **119**, 18 (2014).
- [51] A. Nauts and D. Lauvergnat, Numerical on-the-fly implementation of the action of the kinetic energy operator on a vibrational wave function: application to methanol, *Mol. Phys.* **116**, 3701 (2018).
- [52] G. Avila and E. Mátyus, Toward breaking the curse of dimensionality in (ro)vibrational computations of molecular systems with multiple large-amplitude motions, *J. Chem. Phys.* **150**, 174107 (2019).
- [53] G. Avila and E. Matyus, Full-dimensional (12d) variational vibrational states of CH_4F^- : Interplay of anharmonicity and tunneling, *J. Chem. Phys.* **151**, 154301 (2019).
- [54] G. Avila, D. Papp, G. Czakó, and E. Mátyus, Exact quantum dynamics background of dispersion interactions: case study for $\text{CH}_4\text{-Ar}$ in full (12) dimensions, *Phys. Chem. Chem. Phys.* **22**, 2792 (2020).
- [55] D. Papp, V. Tajti, G. Avila, E. Mátyus, and G. Czakó, $\text{CH}_4\text{-F}^-$ revisited: full-dimensional ab initio potential energy surface and variational vibrational states, *Mol. Phys.* **121**, e2113565 (2023).
- [56] A. Martín Santa Daría, G. Avila, and E. Mátyus, Variational vibrational states of HCOOH , *J. Mol. Spectrosc.* **385**, 111617 (2022).
- [57] G. Avila, A. Martín Santa Daría, and E. Mátyus, Vibrational infrared and raman spectra of HCOOH from variational computations, *Phys. Chem. Chem. Phys.* **25**, 15183 (2023).
- [58] A. Sunaga, G. Avila, and E. Mátyus, Variational vibrational states of methanol (12D), *J. Chem.*

- Theory Comput.* **20**, 8100 (2024).
- [59] C. Qu and J. M. Bowman, Full-dimensional, ab initio potential energy surface for $\text{CH}_3\text{OH} \rightarrow \text{CH}_3 + \text{OH}$, *Mol. Phys.* **111**, 1964 (2013).
- [60] X. Huang, B. J. Braams, and J. M. Bowman, Ab initio potential energy and dipole moment surfaces for H_5O_2^+ , *J. Chem. Phys.* **122**, 44308 (2005).
- [61] B. J. Braams and J. M. Bowman, Permutationally invariant potential energy surfaces in high dimensionality, *Int. Rev. Phys. Chem.* **28**, 577 (2009).
- [62] C. Qu, Q. Yu, and J. M. Bowman, Permutationally invariant potential energy surfaces, *Annual Review of Physical Chemistry* **69**, 151 (2018).
- [63] C. Qu, Q. Yu, B. L. Van Hoozen, Jr, J. M. Bowman, and R. A. Vargas-Hernández, Assessing gaussian process regression and permutationally invariant polynomial approaches to represent high-dimensional potential energy surfaces, *J. Chem. Theory Comput.* **14**, 3381 (2018).
- [64] D. R. Moberg and A. W. Jasper, Permutationally invariant polynomial expansions with unrestricted complexity, *J. Chem. Theory Comput.* **17**, 5440 (2021).
- [65] P. L. Houston, C. Qu, Q. Yu, R. Conte, A. Nandi, J. K. Li, and J. M. Bowman, PESPIP: Software to fit complex molecular and many-body potential energy surfaces with permutationally invariant polynomials, *J. Chem. Phys.* **158**, 044109 (2023).
- [66] M. S. Drehwald, A. Jamali, and R. A. Vargas-Hernández, MOLPIPx: An end-to-end differentiable package for permutationally invariant polynomials in python and rust, *J. Chem. Phys.* **162**, 084115 (2025), 2411.17011.
- [67] J. Bowman, C. Qu, R. Conte, A. Nandi, P. Houston, and Q. Yu, A perspective marking 20 years of using permutationally invariant polynomials for molecular potentials, ChemRxiv; doi:10.26434/chemrxiv-2025-v14p7 10.26434/chemrxiv-2025-v14p7 (2025).
- [68] T. Györi and G. Czakó, Automating the development of high-dimensional reactive potential energy surfaces with the ROBOSURFER program system, *J. Chem. Theory Comput.* **16**, 51 (2020).
- [69] T. B. Adler, G. Knizia, and H.-J. Werner, A simple and efficient CCSD(T)-F12 approximation, *J. Chem. Phys.* **127**, 221106 (2007).
- [70] K. A. Peterson, T. B. Adler, and H.-J. Werner, Systematically convergent basis sets for explicitly correlated wavefunctions: the atoms H, He, B-Ne, and Al-Ar, *J. Chem. Phys.* **128**, 084102 (2008).
- [71] R. Lindh, U. Ryu, and B. Liu, The reduced multiplication scheme of the rys quadrature and new recurrence relations for auxiliary function based two-electron integral evaluation, *J. Chem. Phys.* **95**, 5889 (1991).
- [72] H.-J. Werner, P. J. Knowles, G. Knizia, F. R. Manby, and M. Schütz, Molpro: a general-purpose quantum chemistry program package, *Wiley Interdiscip. Rev. Comput. Mol. Sci.* **2**, 242 (2012).
- [73] H.-J. Werner, P. J. Knowles, F. R. Manby, J. A. Black, K. Doll, A. Heßelmann, D. Kats, A. Köhn, T. Korona, D. A. Kreplin, Q. Ma, T. F. Miller, 3rd, A. Mitrushchenkov, K. A. Peterson, I. Polyak, G. Rauhut, and M. Sibae, The molpro quantum chemistry package, *J. Chem. Phys.* **152**, 144107 (2020).
- [74] H.-J. Werner, P. J. Knowles, P. Celani, W. Györfy, A. Hesselmann, D. Kats, G. Knizia, A. Köhn, T. Korona, D. Kreplin, R. Lindh, Q. Ma, F. R. Manby, A. Mitrushchenkov, G. Rauhut, M. Schütz, K. R. Shamasundar, T. B. Adler, R. D. Amos, S. J. Bennie, A. Bernhardsson, A. Berning, J. A. Black, P. J. Bygrave, R. Cimiraglia, D. L. Cooper, D. Coughtrie, M. J. O. Deegan, A. J. Dobbyn, K. Doll, M. Dornbach, F. Eckert, S. Erfort, E. Goll, C. Hampel, G. Hetzer, J. G. Hill, M. Hodges, T. Hrenar, G. Jansen, C. Köppl, C. Kollmar, S. J. R. Lee, Y. Liu, A. W. Lloyd, R. A. Mata, A. J. May, B. Mussard, S. J. McNicholas, W. Meyer, T. F. Miller III, M. E. Mura, A. Nicklass, D. P. O'Neill, P. Palmieri, D. Peng, K. A. Peterson, K. Pflüger, R. Pitzer, I. Polyak, M. Reiher, J. O. Richardson, J. B. Robinson, B. Schröder, M. Schwilk, T. Shiozaki, M. Sibae, H. Stoll, A. J. Stone, R. Tarroni, T. Thorsteinsson, J. Toulouse, M. Wang, M. Welborn, and B. Ziegler, Molpro, version 2023.2, a package of ab initio programs, see <https://www.molpro.net>.
- [75] E. Anderson, Z. Bai, C. Bischof, S. Blackford, J. Demmel, J. Dongarra, J. Du Croz, A. Greenbaum, S. Hammarling, A. McKenney, and D. Sorensen, *LAPACK Users' Guide*, 3rd ed. (Society for Industrial and Applied Mathematics, Philadelphia, PA, 1999).
- [76] R. Meyer and H. H. Günthard, Internal rotation and vibration in $\text{CH}_2=\text{CCl}-\text{CH}_2\text{D}$, *J. Chem. Phys.* **50**, 353 (1969).
- [77] S. Bell, Variation of geometry, vibrational frequencies and zero-point energies with internal rotation, *J. Mol. Struct.* **320**, 125 (1994).
- [78] G. Avila and T. Carrington, Jr, Nonproduct quadrature grids for solving the vibrational schrodinger equation, *J. Chem. Phys.* **131**, 174103 (2009).
- [79] G. Avila and T. Carrington, Jr, Using nonproduct quadrature grids to solve the vibrational schrodinger equation in 12D, *J. Chem. Phys.* **134**, 054126 (2011).
- [80] E. Mátyus, G. Czakó, and A. G. Császár, Toward black-box-type full- and reduced-dimensional variational (ro)vibrational computations, *J. Chem. Phys.* **130**, 134112 (2009).
- [81] M. H. Cortez, N. R. Brinkmann, W. F. Polik, P. R. Taylor, Y. J. Bomble, and J. F. Stanton, Factors contributing to the accuracy of harmonic force field calculations for water, *J. Chem. Theory Comput.*

- 3**, 1267 (2007).
- [82] D. P. Tew, W. Klopper, M. Heckert, and J. Gauss, Basis set limit CCSD(T) harmonic vibrational frequencies, *J. Phys. Chem. A* **111**, 11242 (2007).
- [83] C. Puzzarini, M. Heckert, and J. Gauss, The accuracy of rotational constants predicted by high-level quantum-chemical calculations. I. molecules containing first-row atoms, *J. Chem. Phys.* **128**, 194108 (2008).
- [84] S. Das and G. Rauhut, Rovibrational calculations without model hamiltonians: The infrared and microwave spectra of thiopropynal, *Int. J. Quantum Chem.* **124**, e27378 (2024).
- [85] G. Rauhut, G. Knizia, and H.-J. Werner, Accurate calculation of vibrational frequencies using explicitly correlated coupled-cluster theory, *J. Chem. Phys.* **130**, 054105 (2009).
- [86] P. Pyykkö, K. G. Dyall, A. G. Császár, G. Tarczay, O. L. Polyansky, and J. Tennyson, Estimation of Lamb-shift effects for molecules: Application to the rotation-vibration spectra of water, *Phys. Rev. A* **63**, 024502 (2001).
- [87] O. Polyansky, A. Császár, S. Shirin, N. Zobov, P. Barletta, J. Tennyson, D. Schwenke, and P. Knowles, High-accuracy *ab initio* rotation-vibration transitions for water, *Science* **299**, 539 (2003).
- [88] B. Temelso, E. F. Valeev, and C. David Sherrill, A comparison of one-particle basis set completeness, higher-order electron correlation, relativistic effects, and adiabatic corrections for spectroscopic constants of BH, CH⁺, and NH, *J. Phys. Chem. A* **108**, 3068 (2004).
- [89] K. Piszczatowski, G. Lach, M. Przybytek, J. Komasa, K. Pachucki, and B. Jeziorski, Theoretical determination of the dissociation energy of molecular hydrogen, *J. Comput. Theo. Chem.* **5**, 3039 (2009).
- [90] M. Siłkowski, K. Pachucki, J. Komasa, and M. Puchalski, Leading-order QED effects in the ground electronic state of molecular hydrogen, *Phys. Rev. A* **107**, 032807 (2023).
- [91] K. Pachucki and J. Komasa, Relativistic correction from the four-body nonadiabatic exponential wave function, *J. Chem. Theory. Comput.* **20**, 8644 (2024), pMID: 39327784, <https://doi.org/10.1021/acs.jctc.4c00861>.
- [92] D. Ferenc, V. I. Korobov, and E. Mátyus, Nonadiabatic, relativistic, and leading-order QED corrections for rovibrational intervals of ⁴He₂⁺ (*x* ²Σ_u⁺), *Phys. Rev. Lett.* **125**, 213001 (2020).
- [93] Á. Margócsy, B. Rácsai, P. Jeszenszki, and E. Mátyus, Rovibrational computations for the He₂ a ³Σ_u⁺ state including non-adiabatic, relativistic, and QED corrections, (under review) arXiv:2506.19116 ((2025)).
- [94] G. Moruzzi, B. P. Winnewisser, M. Winnewisser, I. Mukhopadhyay, and F. Strumia, *Microwave, Infrared, and Laser Transitions of Methanol Atlas of Assigned Lines from 0 to 1258 cm⁻¹* (CRC New York, 1995).
- [95] B. Fehrensen, D. Luckhaus, M. Quack, M. Willeke, and T. R. Rizzo, Ab initio calculations of mode selective tunneling dynamics in C¹²H₃OH and C¹³H₃OH, *J. Chem. Phys.* **119**, 5534 (2003).
- [96] F. Weigend, A fully direct RI-HF algorithm: Implementation, optimised auxiliary basis sets, demonstration of accuracy and efficiency, *Phys. Chem. Chem. Phys.* **4**, 4285 (2002).
- [97] The aug-cc-pVnZ-JKfit series of auxiliary basis sets are unpublished, but included in the basis set library of Molpro 2023. According to their brief description (found in weigend_jkfit_aug.libmol), these augmented JKfit basis sets were generated by them from cc-pVnZ-JKfit by adding one even tempered diffuse function to each primitive set. This was done by building e12/e2 where e1 was the most-diffuse exponent already present and e2 the next most diffuse one if both existed, or e1/2.5 if only one exponent existed beforehand.
- [98] K. E. Yousaf and K. A. Peterson, Optimized auxiliary basis sets for explicitly correlated methods, *J. Chem. Phys.* **129**, 184108 (2008).
- [99] F. Weigend, A. Köhn, and C. Hättig, Efficient use of the correlation consistent basis sets in resolution of the identity MP2 calculations, *J. Chem. Phys.* **116**, 3175 (2002).
- [100] F. Eckert, P. Pulay, and H. Werner, Ab initio geometry optimization for large molecules, *J. Comput. Chem.* **18**, 1473 (1997).
- [101] Geometries with an *ab initio* energy higher than the semihard limit are not rejected outright, but they are only considered for moving into the fitting set if they are required for fixing deep unphysical minima (holes) on the fitted PES. This is detected based on the energy of the PES at the geometry in question, if the PES returns an energy lower than $E_{\text{slopeStart}}$ a hole is assumed.
- [102] Available at <https://www.intel.com/content/www/us/en/developer/tools/oneapi/onemkl.html>.
- [103] Z. Xianyi, W. Qian, and Z. Yunquan, Model-driven level 3 blas performance optimization on loongson 3a processor, in *2012 IEEE 18th International Conference on Parallel and Distributed Systems* (2012) pp. 684–691.
- [104] Q. Wang, X. Zhang, Y. Zhang, and Q. Yi, Augem: automatically generate high performance dense linear algebra kernels on x86 cpus, in *Proceedings of the International Conference on High Performance Computing, Networking, Storage and Analysis*, SC '13 (Association for Computing Machinery, New York, NY, USA, 2013).
- [105] Available at <https://github.com/OpenMathLib/OpenBLAS>.

- [106] T. Gyóri and G. Czakó, ManyHF: A pragmatic automated method of finding lower-energy Hartree-Fock solutions for potential energy surface development, *J. Chem. Phys.* **156**, 071101 (2022).

Supplemental Material

Exact quantum dynamics of methanol: full-dimensional *ab initio* potential energy surface of spectroscopic quality and variational vibrational states

Ayaki Sunaga,¹ Tibor Györi,^{2,*} Gábor Czakó,^{2,†} Edit Mátyus^{1,‡}

¹ *ELTE, Eötvös Loránd University, Institute of Chemistry, Pázmány Péter sétány 1/A 1117 Budapest, Hungary*

² *MTA-SZTE Lendület “Momentum” Computational Reaction Dynamics Research Group, Interdisciplinary Excellence Centre and Department of Physical Chemistry and Materials Science, Institute of Chemistry, University of Szeged, Rerrich Béla tér 1, Szeged H-6720, Hungary*

*tibor.gyori@chem.u-szeged.hu †gczako@chem.u-szeged.hu ‡edit.matyus@ttk.elte.hu

(Dated: 25 July 2025)

S1. CONSTRUCTION OF THE POTENTIAL ENERGY SURFACE

S1.1. *Ab initio* methodology

All *ab initio* electronic structure computations were carried out using the MOLPRO program package (version 2023.2)^{71–74}, with the CCSD(T)-F12b method⁶⁹ and the cc-pVTZ-F12 basis set⁷⁰. All auxiliary basis set options were left at their defaults, resulting in the use of the aug-cc-pVTZ/JKFit^{96,97}, cc-pVTZ-F12/OptRI⁹⁸ and aug-cc-pVTZ/MP2Fit⁹⁹ auxiliary basis sets. Core electrons in the 1s orbitals of C and O were frozen. Optimized *ab initio* geometries were also obtained with MOLPRO¹⁰⁰, at one of the three equivalent minima and torsional saddle points (both have C_s symmetry). MOLPRO’s default integral handling and convergence thresholds are a compromise between execution speed and accuracy, and not optimal for the present work. For this reason, we employed the tighter thresholds summarized in Table S1. An even tighter set of thresholds was employed for the *ab initio* geometry optimizations and harmonic frequency computations, and the convergence thresholds of the geometry optimization were also tightened. The required *ab initio* gradients and Hessians were both obtained via numerical differentiation, and the gradients used a four-point scheme. The MOLPRO output files of the *ab initio* geometry optimizations and frequency computations can be found in the Supplementary Material (harm_freq.tar.lz).

TABLE S1. Global thresholds employed for the *ab initio* computations: PES fitting set (single-point computations) and harmonic frequencies (and the associated geometry optimizations). *oneint* and *twoint* refer to the one-electron and two-electron integration screening parameters, while *compress* refers to a threshold for MOLPRO’s integral compression algorithm. *energy* is a threshold used by MOLPRO to set multiple other thresholds, such as convergence thresholds for Hartree-Fock and post-Hartree-Fock iterations.

	PES	optimization and frequency
oneint	1.0×10^{-14}	1.0×10^{-20}
twoint	1.0×10^{-14}	1.0×10^{-20}
compress	1.0×10^{-14}	1.0×10^{-20}
energy	1.0×10^{-10}	1.0×10^{-12}

S1.2. ROBOSURFER and PES fitting methodology

1. Brief description of the operation of Robosurfer

The PES development was performed using a development version of the ROBOSURFER program system⁶⁸. Without going into the details of the operation of ROBOSURFER, it automates the development of PESs through an iterative, active-learning-like process, which gradually expands

the fitting set with additional samples (geometry-energy pairs) until the quality of the fitted PES is judged to be satisfactory.

We note that besides the fitting set, ROBOSURFER also maintains a secondary set of geometries we call “spares”. These are geometries for which the *ab initio* energy has been computed, but are yet to be moved into the fitting set. The fitting errors of spare geometries are examined by ROBOSURFER every iteration, and any geometry with a weighted (Eq. S3) fitting error greater than the configured target accuracy (E_{targ}) is moved into the fitting set, while geometries already well-described by the PES are left in the spares set.

For this reason, adding geometries to the spares set is the preferred method of expanding the fitting set, as it reduces the risk of accidental imbalanced sampling and the needless inflation of the fitting set. The accumulation of low-error points in the spares set is useful not only for avoiding repeated *ab initio* computations in regions of low fitting error, but some of them can end up moved into the fitting set in subsequent iterations if their weighted fitting error ever exceeds E_{targ} . The brief outline of a single ROBOSURFER iteration is as follows:

1. The PES is fitted based on the geometries in the fitting set, and large numbers of new geometries are rapidly generated using the PES, e.g. by running quasi-classical trajectories (QCT) and geometry optimizations.
2. A set of heuristics is used to estimate which of the new geometries are the most likely to have large fitting errors on the current PES. The most important heuristics are the geometrical and energetic distances of new geometries from the union of the fitting and spare sets. These heuristics select new geometries that are sufficiently different from points already in the fitting set or spares.
3. *Ab initio* computations are performed at the selected geometries and the results (geometries with energies) are appended to the spares set.
4. The fitting error (deviation between the *ab initio* energy and the value of the fitted PES) is evaluated for every geometry in the spares set. If the geometry with the highest weighted fitting error has an error larger than the configured error target, it is moved to the fitting set, a new PES is fitted, and the errors are reevaluated. These “microiterations” are continued until the peak weighted fitting error of the spares drops below the targeted fitting error E_{targ} .

2. General ROBOSURFER configuration and fitting methodology

The PES is fitted using the Braams–Bowman implementation of permutationally invariant polynomials⁶¹. Briefly, the polynomials are expanded in terms of Morse variables, $y_{ij} = \exp(-r_{ij}/a)$, where r_{ij} is the distance between atoms i and j and a is a distance transformation parameter influencing the diffuseness of the polynomial basis. The expansions are truncated by limiting the degrees of the polynomials, as per standard practice. Naturally, this main polynomial expansion includes monomials that may depend on the positions of all N atoms; for this reason, we refer to these as the N -body monomials. The energy expression of the PES is

$$E = \sum_{k=1}^Z c_k T_k M_k, \quad (\text{S1})$$

where Z is the number of permutationally invariant monomials, while c_k and T_k are the coefficient and monomial prefactor of the k -th monomial M_k , respectively.

The flexibility of the fitting function can be further enhanced by the addition of what we call ‘extra monomials’ to the fitting basis. In this work, we use extra monomials obtained with the same polynomial expansion method, but with different distance transformation parameters, maximum degrees, monomial prefactor functions, and a limit on how many atoms they can involve. We group these extra monomials based on the maximum number of atomic positions their expansion may depend on, resulting in 2-body, 3-body, ..., q -body, ..., $N - 1$ -body extra monomials. The prefactors

are usually given by

$$T_k(\mathbf{R}_k, \omega_q) = \begin{cases} \left(1 - \frac{D(\mathbf{R}_k)}{\omega_q}\right)^3 & , \text{ if } D(\mathbf{R}_k) \leq \omega_q \\ 0 & , \text{ if } D(\mathbf{R}_k) > \omega_q \end{cases}, \quad (\text{S2})$$

where \mathbf{R}_k is the subset r_{ij} of interatomic distances the k -th monomial depends on, ω_q is a ‘‘range separation’’ parameter which can be used to smoothly switch off the extra q -body monomials at large r_{ij} , and $D(\mathbf{R}_k)$ is the root mean square (RMS) of the r_{ij} values the k -th monomial depends on. There is one possible special case in prefactor calculation: 2-body extra monomials can be configured to have their prefactors multiplied with $1/r_{ij}$, effectively conferring a hyperbolic shape to these basis functions of the fit, which may improve the description of strong electrostatic interactions such as the repulsive wall at short r_{ij} .

In our experience, for bimolecular reaction PESs it can be beneficial to optimize ω_q for each set of q -body extra monomials separately, however this may result in small unphysical artifacts on the fitted PES near ω_q . For this reason (and since, unlike PES13, we are not aiming to describe the dissociation of methanol), we use $\omega_q = 1000$ bohr in this work for all q . The N -body monomials are given T_k prefactors numerically equivalent to 1 by using $\omega_N = 10^{36}$ bohr for them.

The polynomial coefficients are obtained through weighted linear least squares (LLS) fitting. The weights are computed with a three-segment piecewise function consisting of a constant 1.0 section at low energies, followed by a linear slope intended for reducing the weight of fitting points in somewhat less important regions of the PES, finally ending with a double-hyperbolic section intended to rapidly discount the importance of geometries beyond the maximum energy considered important for the purpose of the PES. The formula for the weight is

$$w(E) = \begin{cases} \frac{E_{\text{dwt},0}}{E + E_{\text{dwt},0} - E_{\text{slopeEnd}}} \frac{E_{\text{dwt},1}}{E + E_{\text{dwt},1} - E_{\text{slopeEnd}}} & , \text{ if } E > E_{\text{slopeEnd}} \\ 1 + \frac{w_{\text{end}} - 1}{E_{\text{slopeEnd}} - E_{\text{slopeStart}}} (E - E_{\text{slopeStart}}) & , \text{ if } E_{\text{slopeStart}} < E \leq E_{\text{slopeEnd}} \\ 1 & , \text{ if } E \leq E_{\text{slopeStart}} \end{cases}, \quad (\text{S3})$$

where E is the *ab initio* energy of the geometry, $E_{\text{dwt},0} = E_{\text{dwt},1} = 0.1$ hartree (21 947 cm^{-1}), $E_{\text{slopeStart}} = 37.2$ kcal/mol (13 011 cm^{-1}), $E_{\text{slopeEnd}} = 45.7$ kcal/mol (15 984 cm^{-1}), and $w_{\text{end}} = 0.75$. E , $E_{\text{slopeStart}}$ and E_{slopeEnd} are relative to the energy at the equilibrium structure. This weight function was also used for weighting the fitting errors of spare geometries when considering if they should be moved into the fitting set. We set the hard upper limit for the energy of geometries that may be included in the fit to 130 kcal/mol (45 468 cm^{-1}) and the semihard upper limit¹⁰¹ to 70 kcal/mol (24 483 cm^{-1}). For solving the LLS equations we use the DGELS and DGELSY LAPACK subroutines, the RCOND condition number threshold of DGELSY is set to 10^{-11} . Over the course of development, we have used both the Intel MKL¹⁰² and OpenBLAS¹⁰³⁻¹⁰⁵ linear algebra implementations.

The ROBOSURFER iterations used two geometry sources: (I) QCT initialized both in the vibrational ground state and with any one of the harmonic vibrational modes excited by one quantum, and (II) geometry optimizations ran on the preliminary fitted PESs. The starting points of the geometry optimizations were randomly chosen from the subset of the fitting set that had an *ab initio* energy $< E_{\text{slopeEnd}}$. We chose not to employ the HOLEBUSTER subprogram for the development of this PES, as it has a tendency to strongly favor the global exploration of configuration space and there is a tradeoff between global fitting accuracy and fitting accuracy in our region of interest near the equilibrium structure.

S1.3. PES development with ROBOSURFER

1. Preparation of the initial fitting set

ROBOSURFER requires an initial fitting set to begin PES development, this was generated using a version of the geometry set generation code first described in Ref. 106. As this program was originally intended for generating datasets of two approaching fragments, we have used a dummy

atom during generation, which was stripped from the resulting geometries before the *ab initio* computations. The *ab initio* optimized minimum geometry was used as the reference geometry. The center of mass distance between the dummy center with a mass of 9 amu and methanol was sampled with 0.01 Å steps between [0.998, 9.608] Å. At each distance, 20 000 random orientations were generated for the methanol and finally the Cartesian coordinates of each geometry were perturbed with random numbers uniformly distributed in $[-0.05, +0.05]$ Å, resulting in a total of 17 240 000 samples before pruning. The pruning step was configured to discard geometries closer than 0.015 to each other in terms of the EW-RMSD ($a = 2$ Å) distance metric⁶⁸, yielding 18 346 initial geometries.

After dummy atom removal and the computation of *ab initio* energies for these geometries 530 of them were randomly chosen to be included in the first fitting set, while the initial spares set consisted of all 18346 geometries.

2. Process of PES development I: initial phase

Over the course of PES development we have taken the approach of starting with a small fitting set, low degree polynomials, and a high fitting error target, then gradually increasing both the flexibility of the fitting function and the accuracy we demand from the PES, as the fitting set grew. We have also followed a heuristic of not using fewer fitting points than 1.5 times the number of polynomial coefficients. We note that the PES is fitted to the total *ab initio* energies, not the relative energies of the fitting set. As a consequence, the RMS errors reported in this subsection are computed from the “absolute” energies returned by the PES, and are therefore inclusive of the errors caused by the shift in the absolute energy of the minimum geometry. Except where otherwise indicated, PESs were fitted using the DGELS LLS solver. Since geometries are always appended to the end of the fitting set, the ordering of them is stable, which lets us use their position in the file as an identifier. For example #200 would be the 201st geometry in the fitting set file, since we are counting from zero. This notation is used below to refer to fitting point that are outliers in the fit (fitting error $> 5 \times$ the RMS fitting error of points in its energy range).

Using the initial geometry sets discussed above, PES development was started with vibrationally ground-state QCT, a primary PI-EW-RMSD geometry selection threshold of 0.013 and a targeted fitting error (E_{targ}) of 1 kcal/mol (349.8 cm⁻¹). Initial fitting parameters were $a = 2.1$ bohr, a 4th degree polynomial fit and no extra monomials, resulting in 317 polynomial coefficients. After 8 iterations, the fitting set grew to 952 geometries and ROBOSURFER was paused.

To hasten the appropriate sampling of PES regions somewhat far from the equilibrium structure, more geometries were generated with the same method that was used for initial geometry generation, except with different parameters: only 10 000 orientations, larger coordinate perturbations in the range of $[-0.1, +0.1]$ Å, and a larger EW-RMSD pruning threshold of 0.0275, which favored the generation of much more dissimilar geometries. This yielded 5 396 geometries, which were appended to the spares set.

ROBOSURFER was then resumed and after 195 more iterations 3 201 fitting points were in use, with a RMS weighted error (RMSWE) of 0.98 kcal/mol, while the spares held 42 979 geometries. As the RMSWE of the fitting set was close to the E_{targ} in use at the time (1 kcal/mol), we considered the fit saturated and increased the polynomial degree to 5, resulting in 1 053 coefficients and a RMSWE of 0.22 kcal/mol.

ROBOSURFER was resumed for another 141 iterations, the fitting set grew to 3 358 geometries and the spares to 57 708, while the RMSWE rose to only 0.28 kcal/mol, giving room for reducing E_{targ} , which was first changed to 0.9 kcal/mol, then over the course of 332 iterations it was gradually lowered to 0.65 kcal/mol, where it was held for 811 iterations. At this point, the fitting and spare sets contained 4 874 and 118 353 geometries, respectively, while the RMSWE of the fitting set had risen to 0.43 kcal/mol, approaching E_{targ} again, prompting us to raise the polynomial degree to 6, yielding 3 250 coefficients.

After 122 more iterations, at fitting and spares set sizes of 5 342 and 120 899 geometries the RMSWE of the fitting set was still only 0.09 kcal/mol, allowing E_{targ} to be lowered to first 0.6 kcal/mol, followed by 83 iterations, then to 0.5 kcal/mol followed by 123 iterations, to 0.4 kcal/mol followed by 123 iterations, to 0.3 kcal/mol followed by 236 iterations, to 0.25 kcal/mol followed by 130 iterations, and finally to 0.23 kcal/mol followed by 549 iterations. At this point the spares set had 134 953 geometries, while the fitting set had 8 097 members and a RMSWE of 0.14 kcal/mol.

Here, we observed that a notable fraction of the outliers in the fit were geometries (Fig. S1) with COH bond angles close to 180° and 90° .

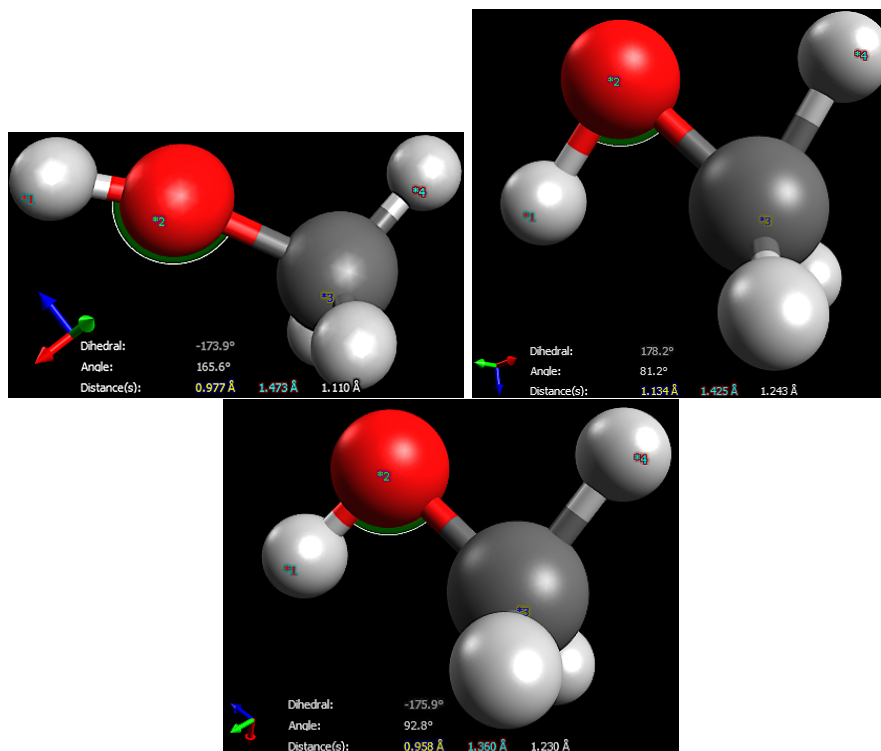


FIG. S1. Geometries of fitting set members which were used for targeted sampling at the early stages of PES development due to their outlier status in the fit. Upper left panel: fitting point #3787, upper right panel: fitting point #8853, lower panel: fitting point #1324.

This prompted us to manually generate additional geometries around one of these outliers (Fig. S1 upper left panel) using the random displacement tool described above, yielding $\sim 3\ 600$ geometries which were appended to the spares. Test fits with different values for a had shown that increasing it to 3 bohr reduced the RMSWE of the fitting set to 0.08 kcal/mol ($\sim 28 \text{ cm}^{-1}$), therefore ROBOSURFER was continued with $a = 3$ bohr for 133 iterations, after which E_{targ} was lowered to 0.21 kcal/mol and 136 further iterations were run. Here, another batch of $\sim 5\ 300$ geometries sampled around an outlier (Fig. S1 lower panel) were appended to the spares. Further increasing a to 3.5 bohr slightly lowered the fitting errors of the fitting set, and 112 iterations were run before the vicinity of a third outlier (Fig. S1 upper right panel) was sampled, and $\sim 3\ 900$ points were appended to the spares. By this time, the RMSWE of the fit had risen to 0.13 kcal/mol, and in an effort to keep the fitting error low a was raised again, to 4 bohr, but this reduced the RMSWE only slightly.

319 iterations later, when the spares set held 148 873 geometries and the fitting set consisted of 12 110 points with a RMSWE of 0.14 kcal/mol, E_{targ} was lowered to 0.2 kcal/mol and 37 more iterations were ran, but by this time the number of new geometries selected in each iteration had fallen greatly, suggesting that the geometries commonly generated by running the geometry optimizer and vibrationally ground-state QCT have mostly been sampled to the density implied by the primary geometry selection PI-EW-RMSD threshold. Therefore, it was reduced from 0.013 to 0.012, allowing more dense sampling. After 29 iterations, E_{targ} was reduced first to 0.19 kcal/mol, then after 53 iterations to 0.18 kcal/mol, followed by 57 further iterations which lead to 155 411 points in the spares and a fitting set with 13 489 points and a RMSWE of 0.15 kcal/mol.

Next, 57 iterations were run with $E_{\text{targ}} = 0.17$ kcal/mol, yielding spares and fitting sets of 157 207 and 14 200 points respectively, but by this time the fitting error of the fitting set had risen quite close to E_{targ} , signaling that the available flexibility of the fitting function in use was again saturated by the fitting set. We considered raising the polynomial degree to 7 (9 343 coefficients), but a test fit with the DGELSY LLS solver showed that the numerical rank of the resulting fitting

matrix would have only been 3 493, i.e. 62% of the monomials would have been ill-determined by the fitting set. While running ROBOSURFER with DGELSY was the straightforward choice to alleviate concerns about the numerical stability of the fit, we were reluctant to take this path due to the slowness of DGELSY and its poor scaling with the number of CPU cores in use.

This prompted us to also check the rank deficiency of the fitting matrix for the 6th degree fit that had been in use, which revealed that only 2 421 out of 3 250 coefficients were strongly determined, forcing us to consider not only the fitting error but also numerical stability while looking for alternative ways of adding flexibility to the fitting function.

3. Process of PES development II: fitting error reduction

First, we attempted to improve the numerical rank of the LLS matrix by continuing PES development with the DGELSY LLS solver, the hypothesis being that discarding the weakly determined monomials could result in higher fitting errors at geometries that would make those monomials more strongly determined, causing their addition to the fitting set. While fitting the 14 200 point fitting set with DGELSY did reveal an outlier (Fig. S2 left panel), moving 100 points into the fitting set did not meaningfully improve the rank deficiency or change the fitting errors. Then, thinking that the last two series of ROBOSURFER iterations might have added suboptimally chosen geometries, the fitting set was truncated back to its 13 489 geometry state, and iterations with DGELSY were run until it again reached 14 300 geometries, but this has not yielded an improvement either and the fitting set was once again reset to 13 489 geometries.

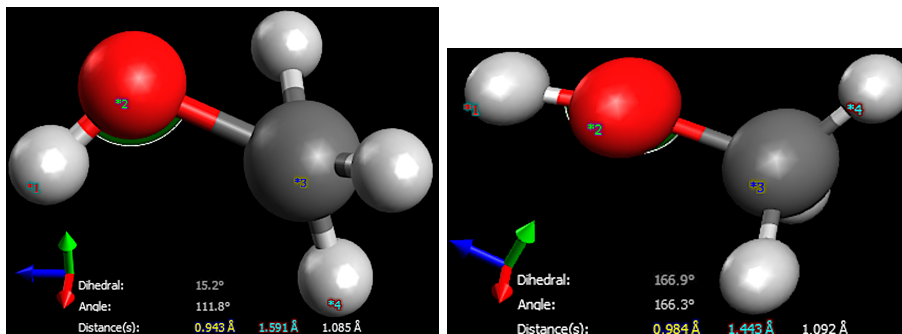


FIG. S2. Geometries of the first pair of fitting set members which were used for targeted sampling at the middle stage of PES development due to their outlier status in the fit. Left panel: fitting point #1736, right panel: fitting point #2055.

After generating ~ 3 400 samples around the outlier in the left panel of Fig. S2 and appending them to the spares set, ROBOSURFER iterations were continued with DGELSY and E_{targ} raised back to 0.19 kcal/mol, until the fitting set grew to 14 401 points, at which point the spares set contained 159 522 geometries. Here the fit had a RMSWE of 0.16 kcal/mol, and we had to accept that approaching our planned fitting accuracy of 10 cm^{-1} would not be possible without a 7th degree main polynomial. Possible explanations for the apparent difficulty of keeping the fitting error of the fitting set low are given in Section 2.2 of the main article.

Test fits done using the earlier 14 200 geometry fitting set had indicated (Fig. S3) that while the simpler DGELS LLS solver (which assumes full numerical rank) favors very large a distance transformation parameters, the more sophisticated DGELSY solver (which only uses the numerically well-conditioned subset of the coefficients) reveals that raising a (which corresponds to a more diffuse polynomial basis) beyond 2-3 bohr makes the fit increasingly ill-conditioned. For the above reasons, we chose to continue with a 7th degree fit, $a = 2.5$ bohr and the DGELSY solver.

This yielded a much lower RMSWE of 0.05 kcal/mol for the 14 401 geometry fitting set, with a numerical rank of 5 942 out of 9 343 coefficients, but several outliers were observed with relative energies < 37.2 kcal/mol. We generated 2 888 additional samples around one of them (Fig. S2 right panel), appended these to the spares set and resumed running ROBOSURFER with the primary PI-EW-RMSD threshold reset back to 0.013, until we reached 16 436 fitting points. One of the original outliers from the 14 401 geometry fit that persisted up to this point (Fig. S4 left panel)

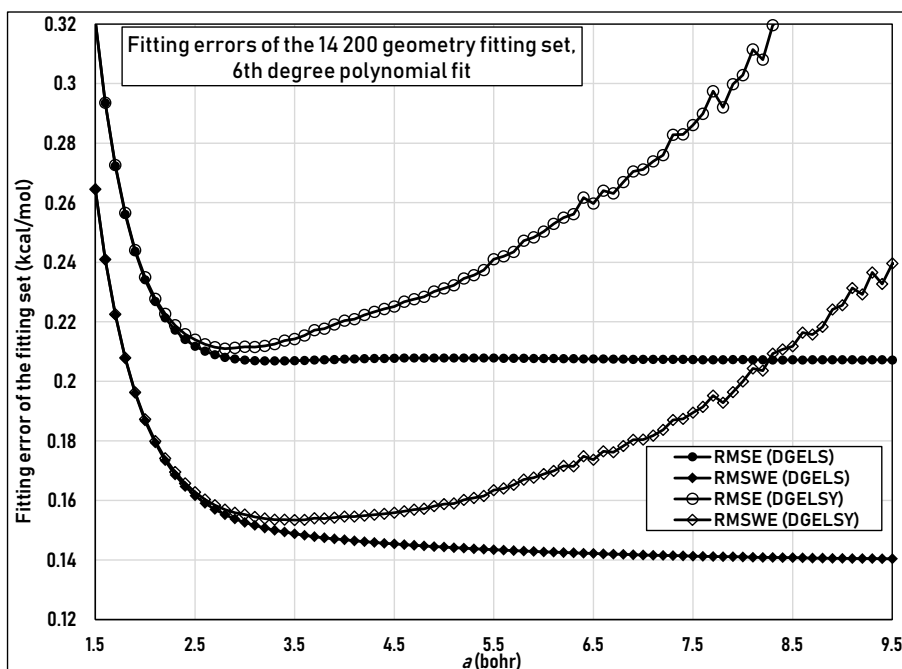


FIG. S3. RMS fitting error and RMS weighted fitting error of a 14 200 geometry fitting set in function of the distance transformation parameter used in the 7th degree fitting polynomial, computed with both the DGELS and DGELSY linear least squares solvers.

was then the subject of the usual targeted sampling, which added $\sim 3\,112$ points to the spares. ROBOSURFER was then continued until the fitting set grew to 17 401 geometries.

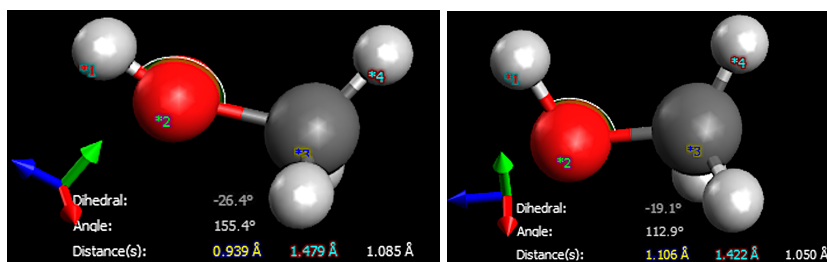


FIG. S4. Geometries of the second pair of fitting set members which were used for targeted sampling at the middle stage of PES development due to their outlier status in the fit. Left panel: fitting point #8197, right panel: fitting point #3655.

Here, the spares set held 163 653 geometries and the RMSWE of the fitting set was 0.07 kcal/mol ($\sim 24\text{ cm}^{-1}$), already much higher than our goal of $\sim 10\text{ cm}^{-1}$. Since further increasing the main polynomial degree to 8 was not practically feasible, we began to increase the flexibility of the fitting function by introducing the extra monomials described in Section S1 S1.2.2, starting with 2-body extra monomials up to 2nd degree. The $1/r_{ij}$ modifier for the 2-body extra monomials was enabled and left enabled until much later in PES development. We performed test fits (Fig. S5) to find optimal values for $a_{2\text{-body}}$ and a and found that the addition of 2-body extra monomials has a very notable effect on the relationship between fitting errors and a , despite the comparatively minuscule number of associated coefficients (12) at 2nd degree. The extra 2-body monomials significantly improve the achievable fitting errors for $a < 3$ bohr and shift the optimal value from ~ 3 bohr to 2.1–2.3 bohr, where the LLS matrix has a much more favorable numerical rank ($\sim 70\%$ rank completeness), as reported by DGELSY.

At this point we experimented with increasing the degree of the 2-body extra polynomial to 5, but as seen on Fig. S5 the changes in fitting errors and rank completeness are both negligible, and the choice of $a_{2\text{-body}}$ between 1 and 3 bohr is similarly inconsequential. Based on these tests, we

continued developing the PES with $a_{2\text{-body}} = 2.5$ bohr and $a = 2.1$ bohr.

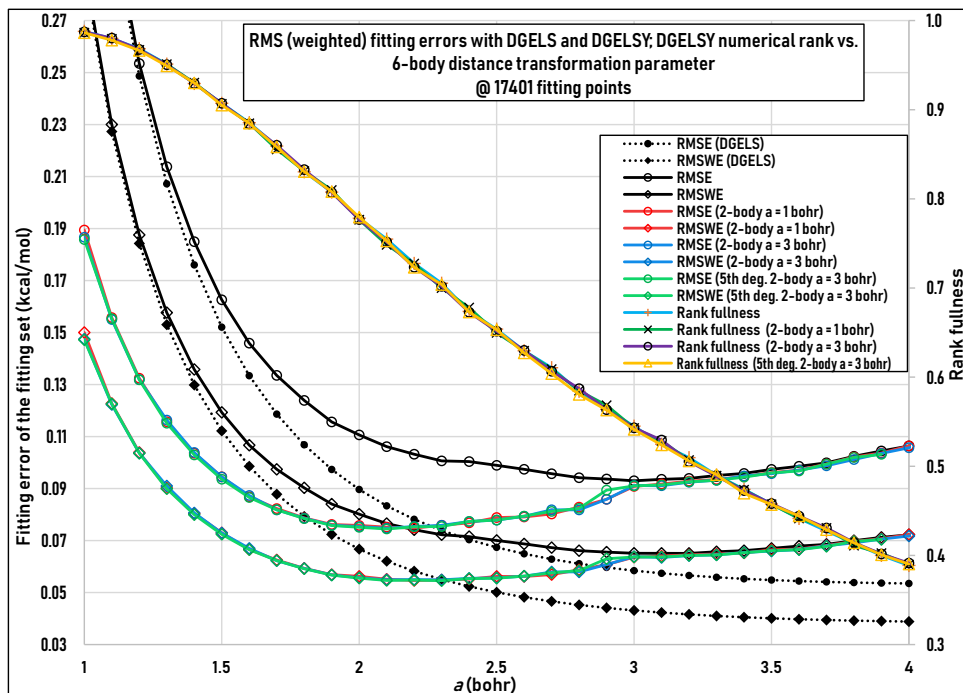


FIG. S5. Left vertical axis: RMS fitting errors and RMS weighted fitting errors of the 17 401 geometry fitting set in function of the distance transformation parameter used in the 7th degree main (6-body) fitting polynomial, computed with the DGELSY linear least squares (LLS) solver unless otherwise indicated. Right vertical axis: ratio between the LLS matrix numerical rank from DGELSY and the number of polynomial coefficients. Curves with no $a_{2\text{-body}}$ indicated belong to fits with no 2-body extra polynomial, curves where only $a_{2\text{-body}}$ is indicated belong to fits with a 2nd degree 2-body extra polynomial.

This initially resulted in an RMSWE of 0.055 kcal/mol (19.1 cm^{-1}), but with multiple outliers. After 1000 geometries had been moved into the fitting set, the RMSWE rose to 21.6 cm^{-1} but only two outliers remained. One of these (Fig. S4 right panel) was chosen for targeted sampling and extra geometries were generated around it as usual, while ROBOSURFER was still running. When the fitting set reached 18 462 geometries, the extra geometries were appended to the spares set of the 17 401 geometry fitting set and ROBOSURFER was resumed with this spares set until there were 19 401 geometries in the fitting set, 166 220 in the spares set, and the RMSWE was 23.6 cm^{-1} .

Here, extra geometries were generated around one of the two outliers (Fig. S6 left panel) that were present in the 19 401 point fit, they were appended to the spares, and ROBOSURFER was resumed with E_{targ} lowered from 0.19 to 0.13 kcal/mol. By the time the fitting set grew to 20 401 geometries, its RMSWE had grown to 25.2 cm^{-1} , prompting us to investigate options for increasing the flexibility of the fitting function again.

Test fits (Fig. S7) confirmed that raising the degree of the 2-body extra polynomial still offered negligible benefits, but adding the 3-body extra polynomial resulted in a substantial reduction in fitting errors (~ 8.8 cm^{-1} RMSWE), even at the 3rd degree where it only contributes 53 coefficients. Just like when the 2-body extra polynomial was added, the shape of the RMSE vs. a curve was altered by the 3-body extra polynomial. The optimal value of a again shifted towards lower values: to 1.9 bohr from 2.1 bohr. This was a welcome change, since reducing a improves the numerical rank of the fitting matrix, furthermore we noted that with the 3-body extra polynomial present, the fitting errors of PESs obtained with the much faster DGELS LLS solver rise much slower at low values of a . The acceptably high DGELSY rank completeness ($\sim 80\%$ at $a = 1.9$ bohr) has allowed us to return to using the much faster DGELS for the rest of the ROBOSURFER iterations in this study, resulting in a RMSWE of 13.1 cm^{-1} for the 20 401 geometry fitting set, if $a_{3\text{-body}}$ is set to 3 bohr and $a_{2\text{-body}}$ is kept at 2.5 bohr.

With these fitting parameters, ROBOSURFER was resumed for 55 iterations, yielding a fitting set of 21 619 geometries, but the rate at which new points were being added to the fitting set was low.

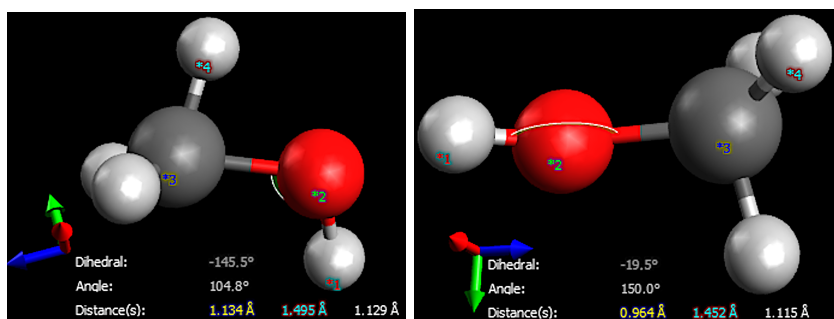


FIG. S6. Geometries of the third pair of fitting set members which were used for targeted sampling at the middle stage of PES development due to their outlier status in the fit. Left panel: fitting point #18507, right panel: fitting point #16520.

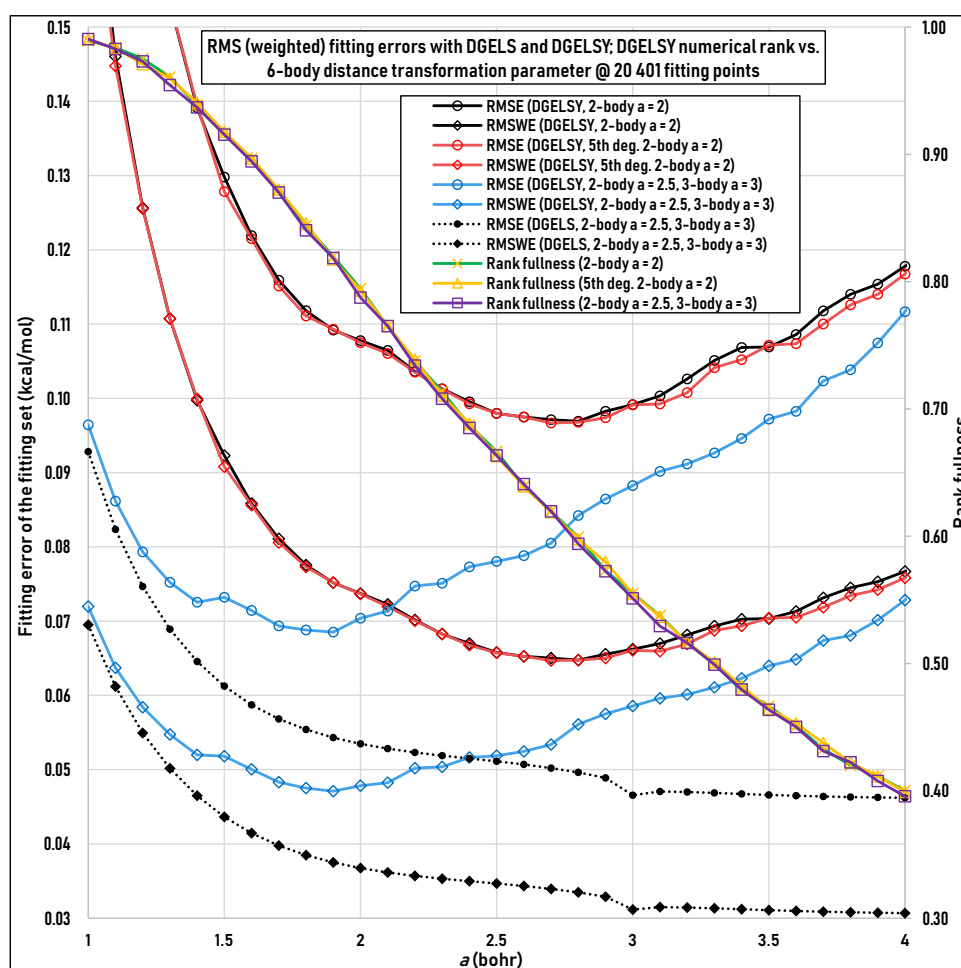


FIG. S7. Left vertical axis: RMS fitting errors and RMS weighted fitting errors of the 20 401 geometry fitting set in function of the distance transformation parameter used in the 7th degree main (6-body) fitting polynomial, computed with the DGELS and DGELSY linear least squares solvers. Right vertical axis: ratio between the LLS matrix numerical rank from DGELSY and the number of polynomial coefficients. Curves with no $a_{3\text{-body}}$ indicated belong to fits with no 3-body extra polynomial, curves where the degree of the 2-body extra polynomial is not indicated belong to fits with a 2nd degree 2-body extra polynomial.

Therefore, a fitting set size of 22 401 was reached by lowering E_{targ} from 0.13 to 0.07 kcal/mol, and from 22 401 geometries, the primary PI-EW-RMSD threshold was lowered from 0.013 to 0.012. When the fitting set reached 24 401 geometries the RMSWE was still only 17.7 cm^{-1} but there were some outliers in the fit, one of which (Fig. S6 right panel) had an *ab initio* energy $< 37.2 \text{ kcal/mol}$, prompting us to generate 3 075 extra samples around it and append these to the spares set.

Development was then continued with $E_{\text{targ}} = 0.085 \text{ kcal/mol}$ and a PI-EW-RMSD threshold of 0.0115 until 26 401 points were in the fitting set, which was achieved in 34 iterations. Here, the RMSWE of the fitting set was 19.1 cm^{-1} , the spares set held 169 370 geometries, and we begun our first attempts at validating the accuracy of the PES using a variety of techniques such as the potential energy curves (PECs) of 1-dimensional slices (Fig. S11 and S12), harmonic vibrational frequency computations, and preliminary variational computations. These indicated that the PES was not satisfactory at 26 401 points, and we aimed to achieve a lower fitting error, leading us to consider our options for increasing the flexibility of the fitting function for the final time.

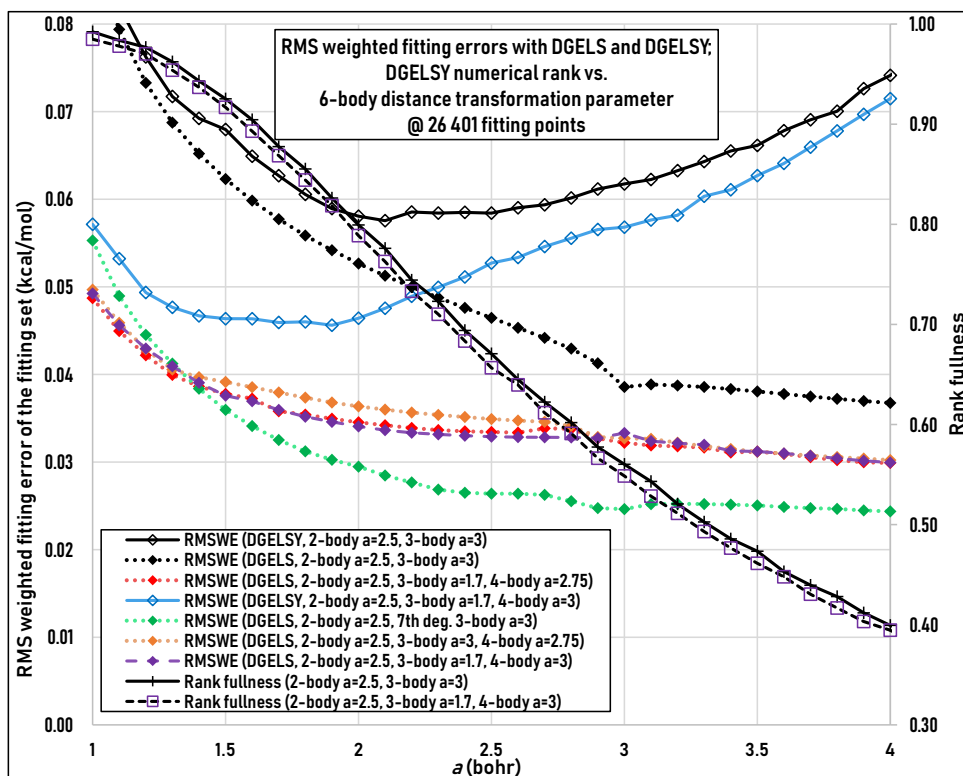


FIG. S8. Left vertical axis: RMS weighted fitting errors of the 26 401 geometry fitting set in function of the distance transformation parameter used in the 7th degree main (6-body) fitting polynomial, computed with the DGELS and DGELSY linear least squares solvers. Right vertical axis: ratio between the LLS matrix numerical rank from DGELSY and the number of polynomial coefficients. Curves with no $a_{4\text{-body}}$ indicated belong to fits with no 4-body extra polynomial, curves where the degree of the 3-body extra polynomial is not indicated belong to fits with a 3rd degree 3-body extra polynomial.

After many test fits (a small subset of which are shown in Fig. S8), we found that while increasing the degree of the 2-body extra polynomial still only had a small effect, expanding the 3-body extra polynomial up to 7th degree did offer a substantial improvement in fitting errors. Introducing the 4th degree 4-body extra polynomial ($a_{4\text{-body}} = 2.75 \text{ bohr}$) instead of increasing the degree of the 3-body extra polynomial yielded a slightly less impressive, but still good improvement in PES fidelity. Despite the lesser improvement, we choose to continue with the introduction of the 4-body extra polynomial, as it changed the RMSE vs. a curve more towards having low fitting errors at the small a values which result in a high numerical rank.

Tuning the values of $a_{3\text{-body}}$ and $a_{4\text{-body}}$ yielded additional reductions in fitting errors, resulting in our final set of distance transformation parameters being $a_{2\text{-body}} = 2.5 \text{ bohr}$, $a_{3\text{-body}} = 1.7 \text{ bohr}$, $a_{4\text{-body}} = 3 \text{ bohr}$, and $a = 1.9 \text{ bohr}$. For the 26 401 geometry fitting set, these parameters achieve

a RMSWE of 16.0 cm^{-1} and a numerical rank of 7 901 out of 9 652 coefficients (82%) when used with the DGELSY LLS solver, and a RMSWE of 12.1 cm^{-1} with DGELS.

4. Process of PES development III: finalization

With the final fitting function and parameters established, ROBOSURFER iterations were continued from the 26 401 geometry fitting set with $E_{\text{targ}} = 0.075 \text{ kcal/mol}$ (26.2 cm^{-1}) and in 17 iterations 2 000 points were added to the fitting set. Here, we noticed an outlier in the lower energy region (Fig. S9), which was used to generate extra samples, and development was continued with $E_{\text{targ}} = 0.07 \text{ kcal/mol}$ (24.5 cm^{-1}) until 29 401 fitting points, where E_{targ} was again lowered to 0.065 kcal/mol (22.7 cm^{-1}).

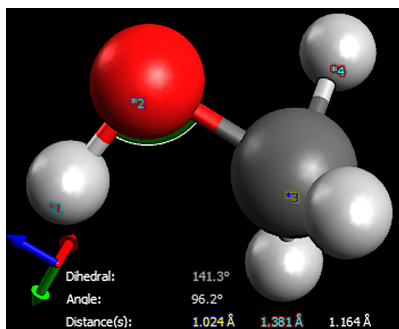


FIG. S9. Geometry #2455 of the fitting set, which was used for targeted sampling at the final stage of PES development due to its outlier status in the fit.

At a fitting set size of 30 401 geometries, where its RMSWE was 14.8 cm^{-1} and there were 171 501 geometries in the spares set, we stopped ROBOSURFER to decide if the quality of the PES was satisfactory and computed a wider set of tests, which included 1D PECs, harmonic frequencies, and a preliminary full-dimensional variational computation (Table S2). Unfortunately, our tests indicated that the vibrational energy levels of the PES deviated more from experimental data than the levels computed with PES13, especially for low energy (within 210 cm^{-1} from the ZPVE) modes, and the harmonic frequencies (Table S3) were also unsatisfactory. This prompted us to continue running Robosurfer, but only 451 geometries were added over 25 iterations, therefore we started lowering E_{targ} in steps of 0.005 kcal/mol to 0.055 kcal/mol (19.2 cm^{-1}), which resulted in the addition of 2 361 geometries to the fitting set in only 38 iterations. At this point, the RMSWE of the fitting set (15.1 cm^{-1}) was quite close to E_{targ} and the RMSE had long exceeded it (24.2 cm^{-1}), therefore we only reduced E_{targ} by 0.874 cm^{-1} before continuing PES development for 21 iterations.

Here, we noticed that some of the trajectories run by ROBOSURFER had been terminating before the number of timesteps we have specified, which was traced down to a quirk of the QCT MD program: since it was originally developed for bimolecular collisions, by default it terminated trajectories where the largest interatomic distance exceeded the largest distance of the initial geometry of the trajectory by $> 1 \text{ bohr}$. This makes perfect sense for terminating reactive trajectories after the products have separated, but since the initial geometry of a monomolecular trajectory only contains short interatomic distances, the vibrational motion can have a large enough amplitude to trigger this termination condition, hindering the effective sampling of large amplitude motions. After fixing this issue, PES development was continued from the 34 186 geometry fitting set with $E_{\text{targ}} = 0.05 \text{ kcal/mol}$ (17.5 cm^{-1}) for 8 iterations, every iteration running 18 trajectories of 500 000 timesteps.

After this, to further focus additional sampling efforts into the vibrationally relevant regions of the PES, the use of vibrationally excited trajectories was implemented in Robosurfer, and 12 of the 18 trajectories in each iteration were started from initial conditions where one of the 12 normal modes were excited by one quantum. This noticeably increased the rate at which new geometries were added to the fitting set, indicating that vibrationally excited trajectories were indeed discovering geometries that are important, but rarely sampled by ground-state QCT. With

TABLE S2. Vibrational energies (relative to ZPVE) of low energy torsional states obtained from preliminary 12-dimensional variational computations with the $b = 4$ basis sets performed using PES fitted to two non-final fitting sets and our final fitting set, compared to energies computed with PES13 and experimental data. The PESs employed in this table were fitted using the DGELS LLS solver. MAE and MAX errors are the mean and maximum absolute differences from experiment. All values are in cm^{-1} .

	PES13 ^a	30 401 geometry fitting set	36 416 geometry fitting set	Final (39 401 geometry) fitting set	Experiment
	9.128	8.842	8.837	8.858	9.122
	9.130	8.844	8.858	8.860	9.122
	208.0	211.6	211.1	210.9	208.9
	208.0	211.6	211.1	210.9	208.9
	292.5	295.6	295.3	295.1	294.5
	353.6	356.1	355.6	355.4	353.2
	509.5	511.8	511.4	511.2	510.3
	509.5	511.8	511.4	511.2	510.3
	749.7	751.6	751.2	751.1	751.0
	749.7	751.7	751.3	751.1	751.0
	1044.7	1044.6	1044.5	1044.5	1046.7
	1045.1	1046.4	1046.0	1045.8	1047.6
MAE	1.1	1.5	1.2	1.1	0
MAX	2.5	2.9	2.4	2.2	0

^aThe values are taken from Table 4 of Ref. 58.

these settings, ROBOSURFER reached the final fitting set size of 39 401 geometries in 52 iterations.

TABLE S3. Harmonic frequencies of methanol (in cm^{-1}) at the equilibrium structure computed using the geometry optimization module of ROBOSURFER (optg) and PESs taken from the final phase of PES development, which were fitted to increasingly numerous geometry-energy pairs. The PESs used in this table were fitted with the DGELS LLS solver, the optimizations and numerical finite difference Hessian evaluations were done in quadruple precision arithmetic due to numerical noise. The reference values were computed with MOLPRO at the *ab initio* level of theory used for PES development, CCSD(T)-F12b/cc-pVTZ-F12. The mean absolute errors (MAE) and maximum absolute errors (MAX) of the harmonic frequencies in cm^{-1} are also listed.

Harm vib. #	Ref. (Molpro)	30 401 geoms.	31 534 geoms.	33 193 geoms.	34 180 geoms.	35 030 geoms.	35 194 geoms.	35 401 geoms.	36 146 geoms.	37 401 geoms.	38 698 geoms.	39 401 geoms.
1	293.1	297.6	298.2	297.5	297.4	297.2	297.2	297.1	297.0	296.4	296.0	295.8
2	1062.2	1061.6	1061.4	1060.8	1060.8	1061.0	1061.0	1060.9	1060.8	1060.7	1060.6	1060.5
3	1090.1	1091.2	1091.2	1091.1	1090.9	1090.9	1090.8	1090.9	1090.8	1091.2	1090.9	1090.9
4	1181.7	1178.0	1178.0	1178.4	1178.8	1178.5	1178.4	1178.2	1177.8	1177.6	1177.4	1177.5
5	1383.7	1376.9	1377.2	1377.4	1377.4	1377.5	1377.6	1377.6	1377.8	1377.8	1378.1	1378.3
6	1485.4	1486.5	1484.3	1485.2	1485.0	1484.5	1484.4	1485.0	1485.3	1485.4	1485.5	1485.7
7	1511.1	1513.2	1512.6	1513.4	1513.0	1512.7	1512.3	1512.3	1512.5	1512.4	1511.9	1512.4
8	1521.6	1524.4	1522.7	1522.6	1522.3	1522.1	1522.3	1522.3	1523.1	1522.7	1522.5	1522.2
9	3015.9	3020.9	3019.5	3019.5	3019.5	3018.6	3018.6	3018.3	3018.8	3017.4	3017.4	3017.4
10	3075.7	3073.7	3072.9	3072.6	3072.5	3072.9	3072.9	3072.7	3073.5	3073.5	3073.7	3073.8
11	3136.7	3132.7	3132.4	3132.6	3132.2	3132.4	3132.3	3132.3	3132.3	3132.9	3133.3	3134.1
12	3866.4	3861.9	3862.2	3862.6	3862.2	3862.8	3862.9	3862.9	3862.8	3863.1	3863.1	3863.1
MAE	0	3.17	2.98	2.87	2.84	2.66	2.63	2.60	2.65	2.41	2.25	2.19
MAX	0	6.82	6.47	6.24	6.24	6.23	6.08	6.12	5.88	5.90	5.62	5.41

Over the course of these iterations, the errors of the harmonic frequencies computed using the PES were regularly evaluated (Table S3), where a slow but steady improvement of the frequencies can be observed, at a rate of approx. 10^{-4} cm^{-1} per fitting set geometry (Fig. S10), which would

have likely continued with further ROBOSURFER iterations.

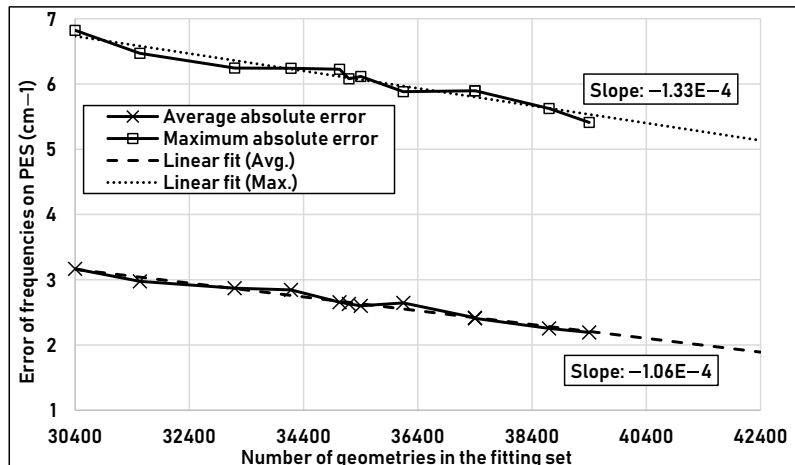


FIG. S10. Evolution of the maximum and average absolute errors of the harmonic vibrational frequencies computed using PESs over the course of the final phase of PES development. These frequency errors belong to PESs fitted with DGELS, the geometry optimizations and numerical Hessian evaluations on the PESs were evaluated using quadruple-precision arithmetic. The reference *ab initio* harmonic frequencies are shown in Table S3.

S2. COMPARISON BETWEEN LINEAR LEAST SQUARES SOLVERS AND POLYNOMIAL EVALUATION PRECISIONS

For the PES fitting process, two LAPACK linear least squares (LLS) solvers are available in the ROBOSURFER code, DGELS and DGELSY. DGELS uses an ordinary QR decomposition assuming that the matrix is full rank. Actual matrices are not full rank, which may warrant the use of DGELSY. DGELSY can handle rank deficiency correctly by performing the QR factorization with column pivoting, but it is much more computationally costly.

Harmonic frequencies computed using different PES variants (DGELS vs. DGELSY, as well as different fitting set sizes and polynomial evaluation precisions of the PES) and the MOLPRO code are listed in Table S4. Attempting to run the geometry optimization with polynomial coefficients from DGELS and double precision polynomial evaluation results in poor convergence of the structure and large values for the rotational and translational frequencies, which should, in theory, become zero as shown by the values for quadruple precision polynomial evaluation. This implies that the PESs fitted using DGELS may include a lot of numerical noise. The coefficients obtained with DGELSY also yield slightly large rotational and translational frequencies in double precision, but to a much lesser extent. Both DGELSY PESs show larger fitting errors for the 1st mode (torsional motion) than the combination of DGELS and quadruple precision evaluation. However, this turned out not to be an issue for our purposes, as evidenced by the good agreement of our torsional computation (Table S7). The harmonic frequencies of other normal modes agree with the MOLPRO values within a few cm^{-1} .

In the GENIUSH computation, the DGELSY PES and double precision polynomial evaluation are employed. Since the center of mass is fixed at the origin of the body-fixed Cartesian coordinate when the PES routine is called, the translational and rotational harmonic frequency would not be a huge matter. However, using quadruple precision for the polynomial in the GENIUSH computation is also a future option because the bottleneck of the variational rovibrational computation is the Lanczos iteration, even if the polynomial is obtained at the quadruple precision.

In MOLPRO, the rotational and translational modes are projected out of the Hessian by default. We also computed the harmonic frequencies without this projection, but the differences between them were only a few $1.0 \times 10^{-2} \text{ cm}^{-1}$ (see `harm_freq.tar.gz` of Supplementary Information).

TABLE S4. Harmonic frequencies of methanol (in cm^{-1}) at the equilibrium structure computed using the geometry optimization module of ROBOSURFER (optg) and various PESs, and the MOLPRO code (CCSD(T)-F12b/cc-pVTZ-F12 and Hessian projection). DGELS and DGELSY are employed as LLS solvers, and double and quadruple precisions are used for evaluating the polynomials when the resulting PESs are used. The labels a-f correspond to the frequencies of rotational and translational motion, while 1-12 correspond to the vibrational harmonic frequencies. The mean absolute errors (MAE) and maximum absolute errors (MAX) of the harmonic frequencies in cm^{-1} are also listed.

#	30401					39401		
	MOLPRO	DGELS doub	DGELSY doub	DGELS quad	DGELSY quad	DGELSY doub	DGELS quad	DGELSY quad
a	0	-102.60	-5.24	-0.04	-0.04	-15.89	-0.04	-0.03
b	0	-51.27	-2.78	-0.02	-0.02	-9.99	-0.02	-0.02
c	0	10.54	4.92	0.01	0.01	-6.14	0.01	0.01
d	0	58.71	5.75	0.01	0.02	-4.35	0.01	0.02
e	0	96.81	8.04	0.03	0.03	-2.98	0.03	0.03
f	0	129.53	13.76	0.04	0.03	8.09	0.04	0.03
1	293.06	302.44	300.53	297.59	300.56	298.73	295.80	298.59
2	1062.17	1061.97	1064.05	1061.62	1064.03	1063.30	1060.48	1063.31
3	1090.10	1099.08	1091.14	1091.21	1091.11	1091.94	1090.90	1091.97
4	1181.67	1177.56	1178.30	1178.01	1178.26	1177.73	1177.48	1177.76
5	1383.68	1382.66	1377.33	1376.86	1377.32	1378.83	1378.27	1378.94
6	1485.40	1486.72	1487.18	1486.51	1487.13	1485.42	1485.75	1485.47
7	1511.08	1514.78	1513.10	1513.20	1513.08	1512.45	1512.40	1512.54
8	1521.64	1526.28	1525.09	1524.37	1525.05	1524.95	1522.20	1524.99
9	3015.85	3022.09	3014.59	3020.86	3014.57	3014.64	3017.37	3014.66
10	3075.65	3076.12	3071.52	3073.74	3071.50	3073.12	3073.78	3073.13
11	3136.65	3139.23	3132.78	3132.72	3132.75	3134.45	3134.11	3134.46
12	3866.44	3862.71	3862.64	3861.91	3862.61	3863.14	3863.11	3863.11
ZPVE	11311.81	11468.46	11309.24	11309.41	11309.10	11309.46	11305.93	11309.57
MAE		3.86	3.37	3.17	3.37	2.61	2.19	2.61
MAX		9.38	7.47	6.82	7.50	5.67	5.41	5.53

S3. ONE-DIMENSIONAL PEC SLICES OF THE FULL-DIMENSIONAL POTENTIAL ENERGY SURFACES

Figures S11 and S12 visualize the potential energy curves (PECs) along the redundant internal coordinates, which are defined in the main text. In these 1D PECs, the other internal coordinates are fixed to the one in an equilibrium structure. The deviations from the *ab initio* energies are also plotted. We can see that deviations from the *ab initio* energy increase at coordinates far from the equilibrium structure, but the maximum deviation is only a few tens cm^{-1} in most of the regions shown in these figures. This indicates that the PES is very well sampled and that holes do not exist in this region at least. The systematic improvement with respect to the number of geometry points is not very obvious from these figures, which would imply that the PESs with fewer fitting set points are already well developed. However, we found that the errors of the harmonic frequencies obtained from the *ab initio* values were gradually decreasing during the PES development. Although the deviation for the torsional paths (10-20 cm^{-1}) is relatively large with respect to the PEC energy (less than 700 cm^{-1}), the torsional energy levels in the vibrational computation agree with the experiment very well (cf. Table S7). Figure S13 is obtained by relaxing other 11D coordinates along the torsional angle. The periodic three minima are reproduced, which provides numerical verification that the permutational symmetry is correctly maintained by the PIP PES.

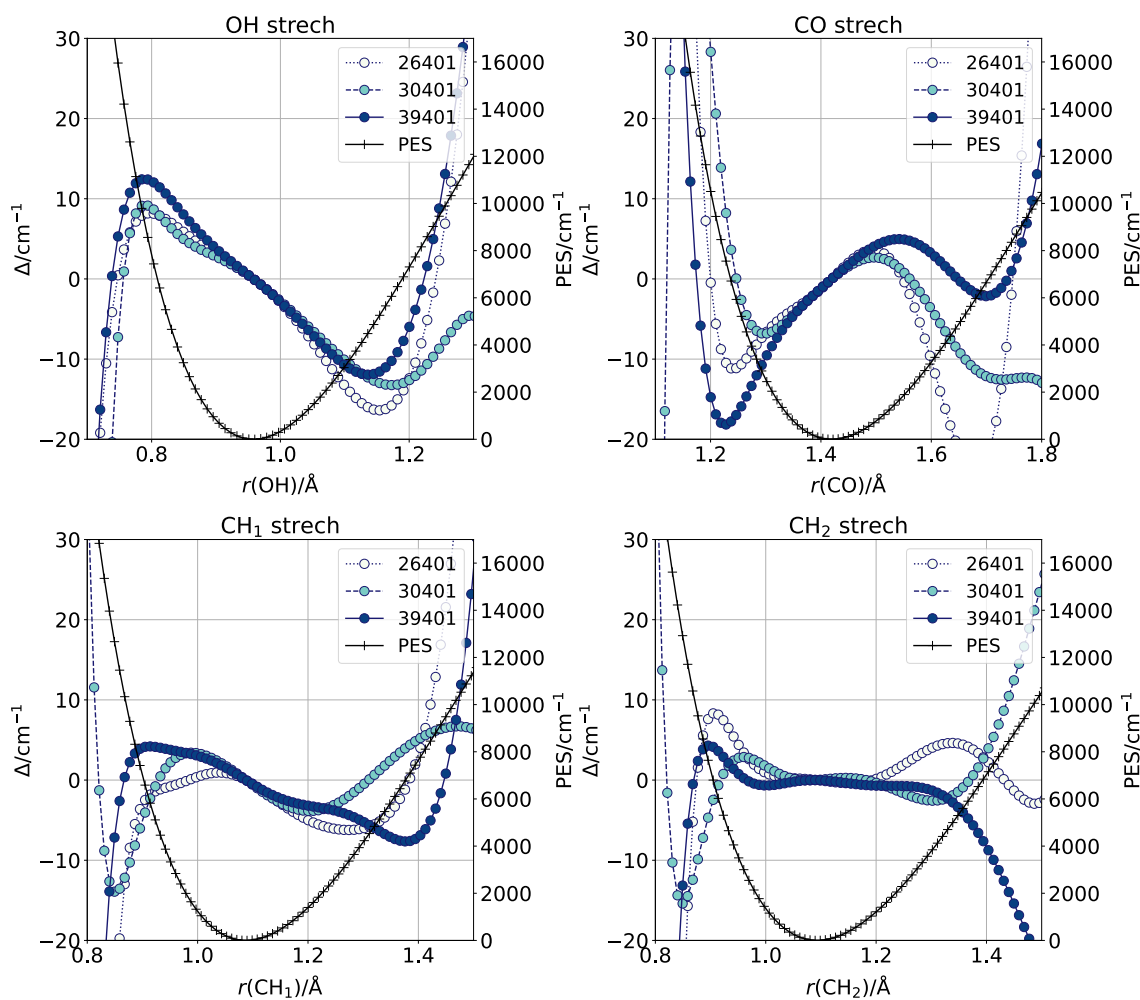


FIG. S11. Evolution of one-dimensional potential energy slices for the non-redundant bond lengths of methanol (cf. Fig. 1 in the main text). The other coordinates are fixed at the equilibrium geometry ($\tau = 180^\circ$) obtained at each PES or *ab initio* calculation. The PESs obtained with the ROBOSURFER (with 26 401, 30 401, and 39 401 geometries in the fitting set) and *ab initio* calculations are shifted so that each minimum value can be zero. The left axis represents the difference between the *ab initio* computations and PESs obtained by the ROBOSURFER (legends: 26401, 30401, and 39401). The right axis represents the *ab initio* PES at the CCSD(T)-F12b/cc-pVTZ-F12 level (legend: PES).

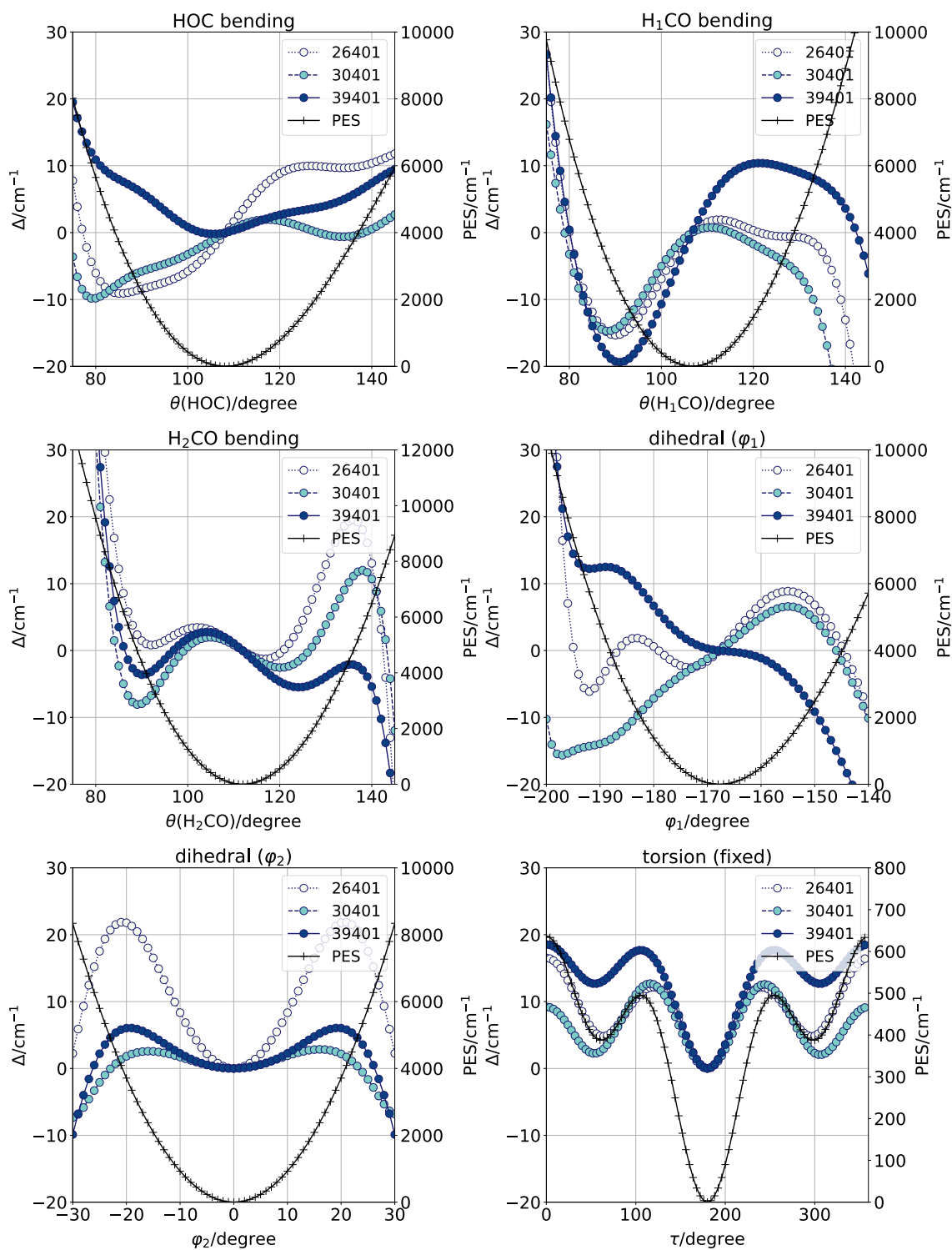


FIG. S12. Evolution of one-dimensional potential energy slices for the non-redundant bond angles of methanol (cf. Fig. 1 in the main text). The other coordinates are fixed at the equilibrium geometry ($\tau = 180^\circ$) obtained at each PES or *ab initio* calculation. The PESs obtained with the ROBOURFER (with 26 401, 30 401, and 39 401 geometries in the fitting set) and *ab initio* calculations are shifted so that each minimum value can be zero. The left axis represents the difference between the *ab initio* computations and PESs obtained by the ROBOURFER (legends: 26401, 30401, and 39401). The right axis represents the *ab initio* PES at the CCSD(T)-F12b/cc-pVTZ-F12 level (legend: PES).

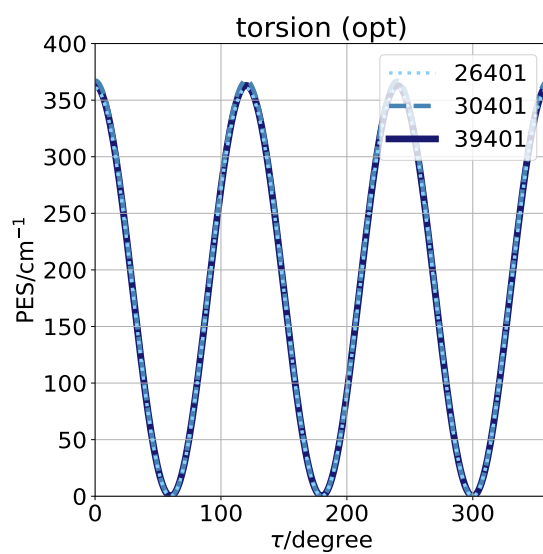


FIG. S13. One-dimensional potential energy slices for the torsional angle of methanol. The other 11D coordinates are optimized at the given torsional angle, and the PES is shifted as the minimum value is zero. The torsional barriers of the PESs with 26401, 30401, 39401 geometry points, and the *ab initio* calculation are 360.8, 367.4, 363.1, and 351.3 (in cm^{-1}) respectively.

S4. EMPLOYED MASSES AND UNIT CONVERSION PERACTOR

In the variational computations, we used atomic masses for the nuclei, $m_{\text{O}} = 15.994\,914\,161\,957$ u, $m_{\text{C}} = 12$ u, $m_{\text{H}} = 1.007\,825\,032\,23$ u. $1 E_{\text{h}} = 219474.63 \text{ cm}^{-1}$ and $1 \text{ u} = 1822.888 m_{\text{e}}$ was employed for the unit conversion, where m_{e} is the mass of an electron.

S5. CONVERGENCE OF THE VIBRATIONAL ENERGIES WITH RESPECT TO THE BASIS SIZE

The effect of the discrete variable representation (DVR) grid points on the torsional energy level is investigated (Table S5). For grid numbers that are multiples of 3 (e.g., 27 and 33 grid points), the degeneracy is improved because the grid points are equally distributed over three equivalent minima. Although some splitting is found for 35 grid points, 33 grid points and functions would be enough to obtain the states up to around 2800 cm^{-1} within the error of 0.1 cm^{-1} .

TABLE S5. Vibrational energy levels of CH_3OH , in cm^{-1} , referenced to the ZPVE (#1) using a 1D vibrational model for an increasing number of DVR grid points. The GENIUSH code and the developed PES using ROBOSURFER (39401 geometries) are used, fitted with DGELSY. The E states whose degeneracies are splitting by more than 0.01 cm^{-1} are highlighted in bold.

DVR	27	29	31	33	35
1	124.555	124.554	124.554	124.554	124.554
2	9.307	9.307	9.307	9.307	9.307
3	9.307	9.308	9.308	9.307	9.307
4	204.769	204.768	204.768	204.768	204.768
5	204.769	204.768	204.769	204.768	204.768
6	291.574	291.570	291.570	291.571	291.570
7	347.470	347.473	347.473	347.473	347.473
8	506.034	506.029	506.034	506.035	506.034
9	506.034	506.041	506.035	506.035	506.036
10	748.255	748.255	748.246	748.256	748.256
11	748.255	748.257	748.266	748.256	748.256
12	1047.569	1047.594	1047.594	1047.608	1047.594
13	1047.884	1047.860	1047.860	1047.845	1047.860
14	1403.021	1402.985	1403.021	1403.021	1403.001
15	1403.021	1403.059	1403.022	1403.021	1403.042
16	1813.635	1813.637	1813.588	1813.636	1813.637
17	1813.635	1813.637	1813.686	1813.636	1813.637
18	2279.070	2279.346	2279.347	2279.317	2279.346
19	2279.639	2279.380	2279.380	2279.408	2279.380
20	2800.064	2799.861	2800.098	2800.098	2800.021
21	2800.064	2800.325	2800.099	2800.098	2800.176
22	3374.243	3375.751	3375.585	3375.786	3375.787
23	3374.243	3375.770	3375.980	3375.786	3375.787
24	3918.838	4004.995	4006.309	4006.284	4006.331
25	4103.253	4005.132	4006.439	4006.497	4006.460

S6. SYMMETRIZATION IN HESSIAN AND COEFFICIENT VECTORS

We developed an algorithm to enforce the numerical symmetry of the Hessian and the coefficient vectors (ave- L). ave- L is obtained using the $\bar{\mathbf{G}}^s$ [and $\bar{\mathbf{F}}^s$] matrices, which are obtained by averaging $\mathbf{G}^s(\tau)$ [and $\mathbf{F}^s(\tau)$] over $\tau = 60^\circ, 180^\circ, 300^\circ$. In this implementation, the symmetrically equivalent vibrational coordinates, degenerate modes, and the number of matrix elements with zero value are considered, which suppress the numerical noises occurring during the GF procedure. This is a more general and stable version to treat symmetry than that we implemented in Ref. 58, which works only with $C_{3v}(M)$.

S7. COMPARISON BETWEEN PES13, PES25, AND EXPERIMENT

Table S6 lists the harmonic frequencies associated with ave- L . The harmonic frequencies obtained using PES13 and PES25 qualitatively agree, but a large deviation is found, e.g., 20.3 cm^{-1} for ν_6 .

TABLE S6. Harmonic frequencies (cm^{-1}) associated with ave- L and their numerical degeneracies. The results of PES25 ($\tilde{\nu}_{25}$) are compared with the values in Ref. 58 using the PES13⁵⁹ ($\tilde{\nu}_{13}$). The corresponding state label and description, the dominant internal coordinates defined in the main text, and the symmetry label in the $C_{3v}(M)$ MS group are also provided. The ν_k , ($k = 1, 2, \dots, 11$) labeling follows the literature convention, corresponding to C_s symmetry, to have comparable assignments for the vibrational states (Tables S7-S9). The ν_k ($k = 1, 2, \dots, 8$) vibrational modes are symmetric, whereas ν_k ($k = 9, 10, 11$) are anti-symmetric for reflection to the COH plane.

state	description	coord	sym	$\tilde{\nu}_{13}$ ⁵⁸	$\tilde{\nu}_{25}$
ν_1	$\nu(\text{OH})$	r_{OH}	a_1	3869.820	3864.309
ν_2	$\nu(\text{CH}_3)_{\text{asym}}$	r_{CH}	e	3104.820	3099.061
ν_9	$\nu(\text{CH}_3)_{\text{asym}}$	r_{CH}	e	3104.820	3099.060
ν_3	$\nu(\text{CH}_3)_{\text{sym}}$	r_{CH}	a_1	3026.114	3024.560
ν_4	$\delta(\text{CH}_3)_{\text{asym}}$	φ_2	e	1510.890	1517.638
ν_{10}	$\delta(\text{CH}_3)_{\text{asym}}$	φ_1	e	1510.887	1517.638
ν_5	$\delta(\text{CH}_3)_{\text{sym}}$	θ_{HCO}	a_1	1475.296	1486.352
ν_6	$\delta(\text{COH})$	θ_{COH}	a_1	1259.733	1280.059
ν_{11}	$\rho(\text{CH}_3)$	θ_{HCO}	e	1196.977	1183.725
ν_7	$\rho(\text{CH}_3)$	θ_{HCO}	e	1196.976	1183.725
ν_8	$\nu(\text{CO})$	r_{CO}	a_1	1066.481	1076.047

Tables S7-S9 list all computed vibrational energies up to 2494 cm^{-1} beyond the ZPVE using the GENIUSH-Smolyak program, the PES13 and PES25 of CH_3OH . The 1st-100th states on PES13 were provided in Table S7 of the Supporting Information of Ref. 58. The other states are newly computed in this study. The detail of the assignment is explained in Section 4.3 in Ref. 58.

We reported in Ref. 58 that our computation for the states (no. 43, 46-47, 48) agreed better with the older experiment reported in 1974¹⁹ than with the more recent experiment reported in 2003²⁴. In contrast, the results for these states of PES25 agree with the experiment in 2003 within a few cm^{-1} . Since the results of PES25 agree with the experiment in the other energy ranges as well, the agreement with the older experiment would be due to the imperfection of PES13. The experimental data were found for all the low-energy states, #2-54, except for the state assigned as $7_1, \nu_\tau = 2, \Gamma = E$ (no. 43-44). If the energy difference between the states #43-44 and #45 is sub- 1 cm^{-1} as shown in our computation on PES25, it would be difficult to assign these two VBOs separately in the experiment.

The vibrational energies obtained in a matrix isolation environment³¹ are shown in parentheses, assuming they are A_1 or A_2 states, except for the doubly-degenerate #150 state. The torsional splitting may be hindered in a matrix environment. The possible matrix effects would be comparable with the discrepancy of our computation from the gas phase experiment, a few cm^{-1} .

TABLE S7. Vibrational energies, $\tilde{\nu}$ in cm^{-1} , referenced to the zero-point vibrational energy (ZPVE, 11119.58 cm^{-1} for PES25, and 11108.05 cm^{-1} for PES13) of CH_3OH in 12D computed with the GENIUSH-Smolyak program with the $b = 7$ basis sets on the PES25 and PES13⁵⁹. Comparisons with the experimental vibrational band origins are also shown. $\delta_X = \tilde{\nu}_{\text{exp}} - \tilde{\nu}_{\text{PES}X}$, in cm^{-1} , where $X = 13, 25$. Assignments are obtained using the wavefunction of PES25's results. SAMs: assignment of the curvilinear normal modes $1_n, 2_n, \dots, 11_n$ ($n = 0, 1, \dots$) in Table S6, zero excitation ($n = 0$) is noted as '0'. '[...]' labels the largest contribution(s) from strongly mixed states. Γ : $C_{3v}(\text{M})$ label according to Table S6 and the status of the torsional part. The details are discussed in Section S1 of the Supporting Information of Ref. 58. All degeneracies for the E states converged better than 0.01 cm^{-1} , except for the pairs listed in the footnotes.

#	ν_τ	SAMs	Γ	PES13	δ_{13}	PES25	δ_{25}	$\tilde{\nu}_{\text{exp}}$
1	0	0	A_1	0.0		0.0		
2-3	0	0	E	9.117	[0.0]	8.856	[0.3]	9.122 94
4-5	1	0	E	208.0	[0.9]	210.9	[-2.0]	208.9 94
6	1	0	A_2	292.4	[2.1]	295.1	[-0.6]	294.5 94
7	2	0	A_1	353.6	[-0.3]	355.3	[-2.1]	353.2 94
8-9	2	0	E	509.3	[1.0]	^d 511.0	[-0.7]	510.3 94
10-11	3	0	E	749.5	[1.6]	750.8	[0.2]	751.0 94
12	0	8_1	A_1	1036.5	[-2.2]	1034.5	[-0.2]	1034.4 22
13-14	0	8_1	E	1045.9	[-3.2]	1043.3	[-0.7]	1042.6 22
15	3	0	A_2	1044.2	[2.4]	1045.4	[1.2]	1046.7 94
16	4	0	A_1	1045.0	[2.6]	1046.5	[1.1]	1047.6 94
17	0	$6_1, 7_1, 11_1$	A_1	1059.7	[15.0]	1074.7	[0.0]	1074.7 22
18-19	0	$6_1, 7_1, 11_1$	E	1064.2	[15.0]	1079.1	[0.2]	1079.3 22
20-21	0	$7_1, 11_1$	E	1154.0	[2.4]	1155.0	[1.5]	1156.5 22
22	0	$7_1, 11_1$	A_2	1163.8	[0.2]	1162.1	[1.9]	1164.0 22
23-24	1	8_1	E	1242.4	[0.6]	1245.8	[-2.8]	1243.0 94
25-26	0	6_1	E	1285.8	[11.7]	1298.2	[-0.7]	^e 1297.5 23
27	0,1	$6_1, 7_1, 11_1$	A_1	1309.8	[10.8]	1319.9	[0.7]	^f 1320.6 23
28	1	$7_1, 8_1, 11_1$	A_2	1322.7	[-2.1]	1320.4	[0.2]	^g 1320.6 23
29-30	1	6_1	E	1336.7	[2.8]	1343.5	[-4.0]	^h 1339.5 19
31	1	8_1	A_2	1328.9	[16.1]	1344.9	[0.1]	ⁱ 1345.0 19
32	0,2	$6_1, 7_1, 11_1$	A_1	1372.8	[-3.1]	1369.3	[0.4]	^j 1369.7 23
33	2	8_1	A_1	1387.5	[1.4]	1392.1	[-3.2]	1388.9 94
34-35	4	0	E	^a 1391.4	[4.8]	1392.2	[4.0]	1396.2 95
36-37	1	$7_1, 11_1$	E	^b 1428.7	[-1.6]	1426.2	[1.0]	^{k,l} 1427.1 23
38	0	5_1	A_1	1444.7	[8.6]	1450.3	[3.0]	^l 1453.3 24
39-40	0	5_1	E	1455.1	[7.0]	1458.7	[3.4]	1462.1 24
41-42	0	$4_1, 10_1$	E	1462.7	[11.2]	1471.7	[2.2]	^l 1473.9 24
43-44	2	$7_1, 11_1$	E	^c 1471.8		1477.4		
45	0	$4_1, 10_1$	A_2	1468.1	[13.4]	1477.8	[3.7]	1481.5 24
46-47	0	$4_1, 10_1$	E	1477.7	[5.6]	1481.8	[1.5]	^l 1483.3 24
48	0	$4_1, 10_1$	A_1	1481.6	[4.5]	1485.4	[0.7]	^l 1486.1 24
49	1	6_1	A_2	1531.6	[9.9]	1541.7	[-0.2]	^m 1541.5 23
50	2	6_1	A_1	1540.7	[6.5]	1547.4	[-0.1]	ⁿ 1547.2 23

^a 1391.400, 1391.415 ^b 1428.660, 1428.673 ^c 1471.807, 1471.820 ^d 511.029, 511.039

^e Assignment of Ref. 23 is $7_1, \nu_\tau = 1, E$.

^f Ref. 23 note that subbands for which one or more of the initial lines that originate from a $\nu_t = 0$ lower level of low energy and low quantum number are observed in the line of ^g

^g Assignment of Ref. 23 is $6_1, \nu_\tau = 0, A$.

^h Ref. 23 also reports another experimental value: 1335.2.

ⁱ Assignment of Ref. 19 is $7_1, \nu_\tau = 1$.

^j Assignment of Ref. 23 is $\nu_\tau = 0, A$, and the SAM is not assigned there.

^k Assignment of Ref. 23 is $\nu_\tau = 1, E$, and the SAM is not assigned there.

^l Ref. 19 also reports experimental values: 1414.0, 1454.5, 1465(3), 1477.2, 1479.5 in cm^{-1} assignable to our no. 36-37, 38, 41-42, 46-47, and 48, energy levels, respectively.

^m Assignment of Ref. 23 is $\nu_\tau = 1, A$, and the SAM is not assigned there.

ⁿ Assignment of Ref. 23 is $\nu_\tau = 2, A$, and the SAM is not assigned there.

TABLE S8. Vibrational states of CH₃OH... [Table S7 continued.]

#	ν_τ	SAMs	Γ	PES13	δ_{13}	PES25	δ_{25}	$\tilde{\nu}_{\text{exp}}$	
51-52	2	8 ₁	<i>E</i>	1543.5	[4.6]	1549.9	[-1.8]	1548.1	94
53-54	1	6 ₁	<i>E</i>	1577.7	[-2.4]	1574.5	[0.9]	1575.3	23
55-56	1,2	5 ₁ , 7 ₁ , 11 ₁	<i>E</i>	1656.3		1661.1			
57-58	1	5 ₁	<i>E</i>	1662.8		1663.9			
59	1	4 ₁ , 10 ₁	<i>A</i> ₂	1668.7		1672.2			
60	1	4 ₁ , 10 ₁	<i>A</i> ₁	1668.0		1682.5			
61-62	1	4 ₁ , 10 ₁	<i>E</i>	1676.6		1685.0			
63	1,2	6 ₁ , 7 ₁ , 11 ₁	<i>A</i> ₂	1712.2		1714.7			
64	2	6 ₁ , 7 ₁ , 11 ₁	<i>A</i> ₁	1745.3		1742.2			
65-66	2	6 ₁	<i>E</i>	^a 1731.9	[10.8]	^b 1742.4	[0.3]	^d 1742.6	23
67	1	5 ₁	<i>A</i> ₂	1748.1		1746.6			
68-69	1	4 ₁ , 10 ₁	<i>E</i>	1756.0		^c 1765.1			
70-71	3	8 ₁	<i>E</i>	1782.3		1778.5			
72-73	5	0	<i>E</i>	1794.7		1803.0			
74	2	5 ₁	<i>A</i> ₁	1809.7		1807.7			
75-76	2	4 ₁ , 10 ₁	<i>E</i>	1819.2		1827.1			
77	3	7 ₁ , 11 ₁	<i>A</i> ₁	1907.6		1909.7			
78	3	7 ₁ , 11 ₁	<i>A</i> ₂	1907.4		1909.8			
79-80	2,3	6 ₁ , 7 ₁ , 11 ₁	<i>E</i>	1942.1		1950.9			
81-82	2	5 ₁	<i>E</i>	1974.8		1963.1			
83-84	2	4 ₁ , 10 ₁	<i>E</i>	1958.9		1969.1			
85	2	4 ₁ , 10 ₁	<i>A</i> ₂	1983.7		1991.2			
86	2	4 ₁ , 10 ₁	<i>A</i> ₁	1985.8		1993.8			
87-88	3	6 ₁	<i>E</i>	1986.6		1997.5			
89	0	8 ₂	<i>A</i> ₁	2060.8	[-5.8]	2058.1	[-3.1]	2055.0	22
90-91	0	8 ₂	<i>E</i>	2070.3	[-6.7]	2066.8	[-3.2]	2063.6	22
92	3	8 ₁	<i>A</i> ₂	2077.1		2080.9			
93	4	8 ₁	<i>A</i> ₁	2077.9		2081.9			
94	0	[6 ₁ + 8 ₁ , 8 ₂]	<i>A</i> ₁	2091.9	[8.4]	2102.2	[-2.0]	^e 2100.2	22
95-96	0	[7 ₁ + 8 ₁ , 8 ₁ + 11 ₁]	<i>E</i>	2096.5	[8.4]	2106.4	[-1.6]	2104.9	22
97	0	[6 ₁ + 7 ₁ , 6 ₁ + 11 ₁]	<i>A</i> ₁	2123.9	[21.2]	2144.8	[0.3]	^f 2145.1	22
98-99	0	[6 ₁ + 7 ₁ , 6 ₁ + 11 ₁]	<i>E</i>	2126.1	[21.3]	2146.9	[0.4]	2147.4	22
100-101	0	[7 ₁ + 8 ₁ , 8 ₁ + 11 ₁]	<i>E</i>	2183.2	[-0.2]	2182.5	[0.5]	^g 2182.9	22
102	0	[7 ₁ + 8 ₁ , 8 ₁ + 11 ₁]	<i>A</i> ₂	2192.8	[-2.2]	2190.1	[0.5]	^h 2190.6	22

^a 1731.850, 1731.861 ^b 1742.346, 1742.378 ^c 1765.133, 1765.145

^d Assignment of Ref. 23 is $\nu_\tau = 2, E$, and the SAM is not assigned there.

^e Assignment of Ref. 22 is $7_1 + 8_1, \nu_\tau = 0, A$.

^f Assignment of Ref. 22 is $7_2, \nu_\tau = 0, A$.

^g Assignment of Ref. 22 is $7_1 + 8_1, \nu_\tau = 0, E$.

^h Assignment of Ref. 22 is $7_2, \nu_\tau = 0, A$.

TABLE S9. Vibrational states of CH₃OH . . . [Table S8 continued.] The subscripts of Ne and N₂ refer to the experimental values obtained in the matrix-isolation spectroscopy in solid Ne and N₂, respectively.

#	ν_τ	SAMs	Γ	PES13 δ_{13}	PES25 δ_{25}	$\tilde{\nu}_{\text{exp}}$
103-104	3	5 ₁	<i>E</i>	2192.8	2203.0	
105	3	4 ₁ , 10 ₁	<i>A</i> ₂	2196.8	2205.8	
106	3	4 ₁ , 10 ₁	<i>A</i> ₁	2196.8	2206.2	
107-108	3,4	7 ₁ , 11 ₁	<i>E</i>	2205.4	2210.4	
109-110	0	7 ₂ , 11 ₂	<i>E</i>	2210.9	2223.8	
111	0,1	[7 ₁ + 11 ₁ , 6 ₁ , 11 ₁]	<i>A</i> ₂	2220.0	2233.7	
112-113	3,4	7 ₁ , 11 ₁	<i>E</i>	2247.6	2234.6	
114-115	3	4 ₁ , 10 ₁	<i>E</i>	2227.9	2235.1	
116	5	0	<i>A</i> ₂	2241.3	2241.4	
117	6	0	<i>A</i> ₁	2241.2	2241.5	
118-119	1	8 ₂	<i>E</i>	2264.4	2267.5	
120	0	[7 ₁ + 11 ₁ , 7 ₂ , 11 ₂]	<i>A</i> ₁	2298.1	2301.6	
121	4	6 ₁	<i>A</i> ₁	2293.0	2306.2	
122	3	6 ₁	<i>A</i> ₂	2294.0	2306.2	
123-124	0	[7 ₂ , 11 ₂]	<i>E</i>	2305.6	2306.3	(2305.0) _{Ne} 31
125-126	0	[6 ₁ + 8 ₁]	<i>E</i>	2314.8	2326.3	
127	1	8 ₂	<i>A</i> ₂	2347.5	2342.2	
128	0	[6 ₁ + 8 ₁]	<i>A</i> ₁	2336.8	2342.3	(2360.2) _{Ne} 31
129-130	1	[6 ₁ + 8 ₁]	<i>E</i>	2364.5	2368.8	
131	1	8 ₂	<i>A</i> ₂	2356.1	2372.0	
132	0	6 ₂	<i>A</i> ₁	2366.6	2383.6	^a (2386.4) _{Ne} 31
133-134	0,1	6 ₂ , 7 ₂ , 11 ₂	<i>E</i>	2377.9	2392.3	
135	0	[7 ₁ + 8 ₁ , 8 ₁ + 11 ₁]	<i>A</i> ₁	2401.0	2397.9	^b (2393.6) _{Ne} 31
136	0	[6 ₁ + 7 ₁ , 6 ₁ + 11 ₁]	<i>A</i> ₂	2383.5	2403.9	
137-138	0,1	6 ₂ , 7 ₂ , 11 ₂	<i>E</i>	2395.3	2410.4	
139	2	8 ₂	<i>A</i> ₁	2409.3	2414.9	
140-141	4	8 ₁	<i>E</i>	2422.6	2426.6	
142-143	1	[7 ₁ + 8 ₁ , 8 ₁ + 11 ₁]	<i>E</i>	2456.8	2452.6	
144	1	[7 ₁ + 11 ₁]	<i>A</i> ₁	2446.0	2453.4	
145-146	0	[6 ₁ + 7 ₁ , 7 ₁ + 11 ₁]	<i>E</i>	2447.1	2461.5	
147	0	5 ₁ + 8 ₁	<i>A</i> ₁	2473.0	2478.9	(2475.2) _{Ne} 31
148	0,1	[6 ₁ + 11 ₁ , 7 ₁ + 11 ₁]	<i>A</i> ₂	2472.0	2481.0	(2489.9) _{Ne} 31
149	0	5 ₁ + 8 ₁	<i>E</i>	2483.6	2487.2	
150	0,2	[6 ₁ + 7 ₁ , 7 ₁ + 11 ₁]	<i>E</i>	2486.5	2494.3	^c (2495.9) _{N₂} 31

^a Assignment of Ref. 31 is 6₁ + 7₁.

^b Ref. 31 does not show the assignment.

^c Assignment of Ref. 31 is 6₁ + 11₁ and 8₁ + 10₁ (doubly degenerate).